Characteristics of bubble clouds at various wind speeds

Magdalena D. Anguelova[1] and Pablo Huq[2]

Received 8 July 2011; revised 1 February 2012; accepted 2 February 2012; published 23 March 2012.

[1] We present the results of a laboratory study on bubble clouds characteristics (length, depth of penetration, width, and void fraction) in fresh water for wind speeds from 9 to 16 m s^{-1}. Temporal and spatial changes of these characteristics and their statistics were extracted from video images from side and top views. Cloud characteristics were scaled with the period T, wavelength L, phase speed c, and significant wave height H_s of the dominant wave. The lifetime of the bubble cloud comprises formation, growth and decay stages. The bubble cloud moves forward horizontally with the wave for the initial 1/3 of the wave period at approximately half the wave phase speed ($0.5c$). The subsequent dominant motion of the bubble cloud in the wave trough is vertical with a mean speed half that of rising bubbles. The void fraction is as high as 80–99% in the first quarter ($0.25T$) of the bubble cloud lifetime corresponding to wave phase of up to 90°. The void fraction decreases steadily to about 20–30% at $0.7T$ (wave phase of ~270°). Probability density functions of the bubble cloud characteristics show that the bubble cloud length varies from $0.1L$ to $0.7L$; the bubble cloud thickness ranges from $0.5H_s$ to $2H_s$. Scaled bubble cloud characteristics and the cloud void fraction vary weakly with the wind speed for the growth stage. Residual void fractions can persist for long times $O(100T)$.

Citation: Anguelova, M. D., and P. Huq (2012), Characteristics of bubble clouds at various wind speeds, *J. Geophys. Res.*, *117*, C03036, doi:10.1029/2011JC007442.

1. Introduction

[2] Bubble clouds form when wind-generated waves break in the open ocean and entrain air into the water. The geometry, kinematics, and dynamics of the bubble clouds are highly variable in space and time. Two factors are primarily responsible for the variability of the bubble clouds—the wavefield and the evolution of the entrained air. The wavefield affects the bubble clouds through the variations of the rate, scale (e.g., wave height), and intensity (e.g., wind-forcing) of the wave breaking caused by various environmental and meteorological conditions. After wave breaking, the evolution of the entrained air affects bubble clouds through various processes, e.g., changes in bubble sizes, bubble buoyancy, etc. Immediately after wave breaking, the bubbles in clouds cover a wide range of sizes but with a prevalence of large radii, e.g., above 0.4 mm and up to 4 mm [*Lewis and Schwartz*, 2004, chapter 4.4]. The largest bubbles, being more buoyant, rise to the surface quickly and burst. Bubbles with smaller sizes may live long enough to spread horizontally or penetrate deep in the water column, to shrink and equilibrate with the hydrostatic pressure, to dissolve due to combined effect of the hydrostatic pressure and surface tension, and to stabilize against further dissolution when fully coated by surface-active materials. The saturation levels of dissolved nitrogen and oxygen in the surface layer of the ocean can additionally influence the fate and number of small air bubbles [*Stramska et al.*, 1990]. The spatial and temporal variations of the bubble clouds below the air-sea interface are visible on the ocean surface as whitecaps which form, grow, and decay.

[3] Though short-lived and patchy, bubble clouds and whitecaps are important in air-sea interaction. For example, the presence of bubble clouds causes energy dissipation and turbulent mixing in the upper ocean [*Melville*, 1996]; bubble clouds produce sea spray and aerosols which influence climate [*Blanchard*, 1963; *Monahan et al.*, 1982; *de Leeuw et al.*, 2011]; contribute to heat exchange and intensification of tropical cyclones [*Fairall et al.*, 1994; *Andreas et al.*, 2008]; enhance gas transfer of climate relevant gases across the air-sea interface [*Thorpe*, 1982; *Woolf*, 1993; *Wanninkhof et al.*, 2009]; change the sound speed and the ocean ambient noise [*Prosperetti*, 1988]; alter the optical properties of the water [*Koepke*, 1986; *Frouin et al.*, 1996] thus affecting the retrievals of ocean color [*Gordon and Wang*, 1994]; complicate the sea state thus reducing the accuracy of retrieving wind velocity [*Swift*, 1990] and salinity [*Camps et al.*, 2005] with active and/or passive microwave measurements.

[4] The bubble size distribution (defined as the number of bubbles per unit volume per radius band) is needed to quantify various air-sea interaction processes and thus has been extensively measured. Field measurements made at different wind speeds, depths, and instrument resolution and laboratory studies under well controlled conditions have

[1]Remote Sensing Division, Naval Research Laboratory, Washington, DC, USA.
[2]College of Earth, Ocean, and Environment, University of Delaware, Newark, Delaware, USA.

helped better understand the role of various factors such as wind speed, water temperature, salinity, and surfactants on bubble size distributions [*Monahan and O'Muircheartaigh*, 1986; *Carey et al.*, 1993; *de Leeuw et al.*, 2011]. However, most techniques for bubble sizing reach their effective limit upon encountering the high concentration of bubbles within bubble clouds immediately after and beneath breaking waves [*Lamarre and Melville*, 1992; *Leifer et al.*, 2003a]. High concentrations diminish the sensor's ability to distinguish the individual bubbles and to measure a wide range of bubble sizes precisely. Because bubble size distributions are used to determine bubble cloud void fraction α (defined as the volume occupied by the bubbles in a unit volume of air/water mixture), if such distributions are unavailable, direct measurements of α are an alternative approach for the high concentrations in the early stages of wave breaking.

[5] We report the experimental results of a laboratory investigation of the geometric and kinematic characteristics and void fraction of bubble clouds for a range of wind speeds (9–16 m s^{-1}) at a fixed water temperature of 20°C in tap water with a photographic technique. The bubble cloud dimensions of length l and thickness d are well resolved in side view images of the water body along the tank. The bubble cloud width w across the tank is observable from top view images. Temporal and spatial variations of the bubble cloud dimensions and void fraction are tracked. The bubble cloud characteristics are scaled with the corresponding wave characteristics. Most previous laboratory measurements have been conducted with mechanically generated waves. There are two experiments which used wind generated waves, but they were for one wind speed only (section 2.3). This study covers a wider range of wind speeds.

2. Background

[6] Difficulties in measurements have prevented detailed study of the processes taking place in the vicinity of the wave crest during breaking. Measurements of bubble cloud characteristics *en mass*e are challenging, and counting and sizing of individual bubbles during the initial stage of breaking were not possible until recently. As a result, little data are available for the transient bubble population from breaking compared to data of the background bubble population. Here we review measurement techniques and previous results of characteristics of bubble clouds such as dimensions, shape, and void fraction.

2.1. Bubble Cloud Measurement Techniques

[7] Three measuring techniques have been widely used for counting and sizing bubbles [*Leifer et al.*, 2003a; *Lewis and Schwartz*, 2004]—optical, photographical, and acoustical. These techniques provide void fraction values indirectly as the total amount of air entrained by breaking waves is obtained either by summing the bubble size distributions or by inverse algorithms. However, these techniques do not resolve individual bubbles in dense, transient clouds. The need to resolve high void fractions has motivated the application of measurement techniques used in the study of two-phase flows in fluid dynamics and industrial processes. These are "medium-based" techniques and they measure the void fraction directly.

[8] No single technique provides adequate measurements over wide range of bubble sizes, in a large sampling volume, and over a large spatial area [*Su et al.*, 1994]. Rather, a combination of techniques is required to fully characterize bubble clouds [*Vagle and Farmer*, 1998]. The principles of operation of the various systems largely determine the sampling volume and the range of bubble sizes or void fractions measured. Optical systems register the specular reflection and/or scattering of light by the bubbles. Photographic systems record images of the bubbles visualized with various lighting schemes (see section 2.5). Acoustical techniques use various methods based on the attenuation of sound by bubbly mixtures, e.g., acoustic resonator [*Medwin and Breitz*, 1989]; the modification of the sound speed by the presence of bubbles [*Terrill and Melville*, 1997]; and sound backscatter [*Thorpe*, 1982; *Vagle and Farmer*, 1992]. "Medium-based" techniques rely on variations of properties of the media such as impedance (measured by a conductivity probe) or refractive index (measured by a fiber optic probe) [*Cartellier*, 1990].

[9] Indirect estimates of bubble cloud void fractions with optical, photographical, and acoustical techniques are prevalent and continue to improve. For example, *Stokes and Deane* [1999] devised an imaging system that operates in the interior of the dense bubble plume yet maintaining an optically clear path between the recording camera and the scattering bubbles in the sampling volume. *Kalvoda et al.* [2003] and *Leifer et al.* [2003a] combined two and more cameras to observe both bubble plumes and individual bubbles. However, direct measurements are becoming increasingly accurate. *Lamarre and Melville* [1992, 1994] utilized a conductivity probe to directly measure void fractions above 1% (section 2.3). A constraint of this technique when used in the vicinity of breaking wave crests is signal saturation when the conductivity probe crosses the water surface—surface effect; this requires signal processing to remove saturated data. *Rojas and Loewen* [2007] and *Blenkinsopp and Chaplin* [2007] demonstrated the use of fiber optic probes to obtain both direct measurements of high void fractions (up to 100%) and bubble size distributions. Other principles of operation could expand the possibilities for direct void fraction measurements. For example, *Monahan et al.* [1994] developed a mechanical void fraction meter to directly obtain void fraction via application of the ideal gas law. The potential of this simple mechanical meter can be improved by miniaturizing the device so that it would be less intrusive to the surrounding turbulent flow, but keeping the sampling volume sufficiently large to provide a meaningful average void fraction measurement (E. C. Monahan, personal communication, 2012).

[10] Each measurement technique has advantages and disadvantages. *Su et al.* [1994] compared optical, photographical and acoustical techniques and concluded that the optical technique was the most accurate in determining the bubble sizes in their range of application. *Vagle and Farmer* [1998] evaluated three different acoustical systems and the conductivity probe and found that acoustical methods are most suitable for long-term monitoring of bubble clouds because they are sensitive to low void fraction values, from 10^{-9} to 10^{-4}. Other advantages of acoustical systems relative to optical and photographic systems are larger sampling volume and amenability to automation of the data processing [*Su et al.*, 1994].

A drawback of the acoustical techniques is that they are indirect measurements of void fraction and require either careful calibration and/or inversion algorithms. It is expected that their use in conjunction with direct void fraction measurements, e.g., by a conductivity probe, would alleviate this drawback [*Vagle and Farmer*, 1998]. A major drawback of photographic systems has been the difficulty of automating the analysis of images [*Su et al.*, 1994]. However, *Stokes and Deane* [1999] and *Leifer et al.* [2003a] have shown that automation of the image analysis is feasible. Therefore, photographic techniques have become attractive for the evaluation of high void fractions and cloud dimensions. Fiber optic probes have the potential for accurate measurements of wide range of void fractions [*Rojas and Loewen*, 2010].

2.2. Field Measurements of Bubble Cloud Characteristics

[11] Void fraction values α can be obtained from bubble size spectra measured in the field with a photographic technique. *Bezzabotnov* [1985] measured bubble size distributions at the air-sea interface and 10 cm below in the cold (5°C to 8°C) brackish (8–13 psu) waters of Baltic and Caspian seas under wind speeds from 7 m s^{-1} to 16 m s^{-1}. From these, he obtained densities of the two-phase mixture of the bubble clouds ranging from ρ_m = 886 kg m^{-1} at the interface to ρ_m = 999 kg m^{-3} at 10-cm depth. Because ρ_m is a linear combination of the densities of the seawater and air (ρ and ρ_a, respectively), i.e., $\rho_m = \alpha\rho_a + (1 - \alpha)\rho$ [e.g., *Odelevskiy*, 1951], one can use ρ_m values to estimate α. Using the same value of ρ = 1000 kg m^{-3} which Bezzabotnov used and choosing ρ_a = 1.27 kg m^{-3}, we find the void fractions equivalent to the reported ρ_m values to be 0.1% to 3% for bubble clouds at 10 cm depth and 11% for the foam at the interface. Subsequently, *Bezzabotnov et al.* [1986] conducted similar experiments at 10 cm depth in the warmer (~20°C), saltier waters of the Pacific Ocean under wide range of wind speeds, from 9 m s^{-1} to 20 m s^{-1}. The reported ρ_m values translate to void fractions of the bubble clouds from 0.05% to 7.7%. The doubling of void fraction α, as compared to the previous results [*Bezzabotnov*, 1985], was likely due to higher salinity. *Bezzabotnov et al.* [1986] observed markedly different bubble characteristics and behavior for the bubble populations in the initial breaking stage as compared to later (1–3 s after the breaking) stages. For example, bubbles have considerably higher velocity, from 60 cm s^{-1} to more than 100 cm s^{-1}, immediately after breaking, and are almost motionless in later stages. *Walsh and Mulhearn* [1987] also measured bubble size spectra with a photographic technique and used them to obtain void fraction α. They reported much lower values of α ranging from 10^{-8} to 10^{-6} depending on the wind speed (2–14 m s^{-1}) and depth (0.5–2 m). These were void fraction values more representative for the background bubble population than for the transient bubble populations observed by *Bezzabotnov* [1985] and *Bezzabotnov et al.* [1986]. But even the void fractions of the background bubble population were highly variable in time with large deviations from the mean values. *Deane* [1997] used two sets of underwater photographs taken in the surf zone to describe the bubble plumes and the individual bubbles a few seconds after the wave breaking at depth of about 0.5 m. The "plume" photographs revealed bubbles "so densely packed that they had the appearance of a solid mass" [*Deane*, 1997, p. 2675] with void fractions as high as 0.3–0.4 obtained from bubble size spectra. Subsequently, *Deane and Stokes* [1999] report a time scale of 90 ms or less for the disintegration of the compact air-water mixture to individual bubbles tractable to counting and sizing.

[12] The various acoustical techniques provide void fraction values for the background bubble population. Thorpe and coworkers observed the shapes and the penetration depths of clouds of bubbles below the surface with an upward-pointed sonar in a series of field experiments [*Thorpe*, 1982, 1992]. The depth of penetration of the bubble cloud increased with wind speed to values of 1–4 times the significant wave height. The time-averaged value of bubble density, inferred from acoustic scattering, decreased exponentially with depth. *Melville et al.* [1995] reported values of void fractions of 10^{-6} to 10^{-4} at 0.7 m depth during a storm event in the North Atlantic. Time averaged (over 40 min) void fraction values were determined from measured sound speed using Wood's relationship between sound speed and void fraction [*Terrill and Melville*, 1997]. *Dahl and Jessup* [1995] recorded video images of the sea surface and measured time varying properties of subsurface bubble clouds with an acoustic device. They estimated the phase speed of the breaking waves from video records, and their characteristic length λ_c and time T_c were derived from a dispersion relation. These were used to scale the spatial and temporal characteristics of the clouds. The entrainment depth of the bubbles was presented for times after $3T_c$. They propose an empirical expression $D/\lambda_c \propto (t/T_c)^{0.7}$ to describe the evolution of the bubble cloud with the depth. Values of void fraction of order 10^{-8} at a depth of 1.5 m were calculated from the acoustic backscattering cross section.

[13] *Lamarre and Melville* [1992] have demonstrated the feasibility of the conductivity probe for measurements of the void fraction in the field. The experiments were conducted off the coast of Delaware under wind speeds from 4 m s^{-1} to 15 m s^{-1}. A vertical line of conductivity probes at various depths recorded void fractions up to 24% at a depth of 20 cm and about 4% at 50-cm depth.

2.3. Laboratory Measurements of Bubble Cloud Characteristics

[14] *Longuet-Higgins and Turner* [1974] used laboratory data on air entrainment to build and verify a model for the whitecap formed by a spilling breaker. Their model considers the whitecap as a turbulent flow riding on the slope of laminar flow. The motion of the whitecap down the slope of the wave is driven by a density difference formed by entrainment of the non-turbulent fluid of the wave into the turbulent region of the lighter whitecap. The model's prediction that a density difference greater than 8% sustains a steady motion of the whitecap near the crest of the breaking wave is in accord with observations of spilling breakers. A limitation of the model is that the assumption of quasi-steady breaking is not always valid for the highly intermittent breaking process.

[15] *Bonmarin* [1989] investigated the shape evolution of mechanically generated steep waves in fresh water up to and after the breaking stage using a photographic technique. The results demonstrated and quantified the marked asymmetry of the wave crest just before breaking; visualized the formation of an elliptical region of air by the overturning jet of

a plunging breaker; and described the splash-up occurring as a consequence of the interaction between the overturning jet and the undisturbed wave surface. Time series of the vertical elevation and distances traveled by the wave crest and the splash-up, normalized by the wave characteristics, were presented.

[16] *Lamarre and Melville* [1991, 1992] measured the air entrained by mechanically generated deep water breaking waves with a conductivity probe in a 2-D (0.76 m wide) wave channel filled with fresh water. The bubble clouds moved at or near the phase speed of the wave immediately after breaking. They observed void fractions over the full range 0–100% (excluding the surface effect of the conductivity probe, section 2.1) with values of 100% for the initial air pocket. Void fractions as large as 20% were sustained for approximately half of the wave period, and did not decrease below 1% during the entire wave period. *Lamarre and Melville* [1994] measured the void fraction in bubble plumes generated by breaking waves in fresh water in a large 3-D (30.5 m wide) basin. A vertical array of six conductivity probes recorded data from the still water level (SWL) to a depth of 75 cm. The void fraction in a cross section of the bubble plume at the centerline of the basin ranged from 0.3% up to about 50%. The results of the 3-D experiment were comparable to those of the 2-D experiment for times up to about half the wave period. Differences in the results for later times were explained by entrainment of more fluid into the bubble cloud from the side in the 3-D case as compared to the more constrained conditions of the 2-D case.

[17] *Loewen et al.* [1996] used a photographic technique to measure size distributions of large bubbles (radii up to 3 mm) formed by mechanically generated breaking waves in fresh and salt water at a temperature of 21°C. Void fractions of the order of 0.13% and 0.26% were obtained from the bubble size distributions in fresh and salt water, respectively. *Kalvoda et al.* [2003] characterized clouds of large bubbles produced by breaking waves at wind velocity of 16 m s^{-1} in a laboratory tank using a photographic system. Temporal evolution of the cloud dimensions (length, aspect ratio, and area) and velocity were evaluated from side and top views. The maximum cloud lengths in the top and side views were 0.1 and 0.16 of the wavelength, respectively, and the maximum penetration depth approached one half the wave height. The average horizontal cloud speed was about 0.45 times the phase speed of the wave, with initial values ranging from one half to two thirds of the phase speed. The void fraction, calculated from the size distributions, was about 0.4% for the air-water volume estimated as the product of side view area and the top view width of the cloud.

[18] *Leifer et al.* [2006] and *Leifer and de Leeuw* [2006] used a photographic system to study bubble plumes and individual bubbles in the plumes formed by breaking waves in a wind-wave tunnel under wind speed of 13 m s^{-1} additionally forced by a mechanical paddle. The measurements were made at various fetches (17.5–30 m) in fresh water with water temperatures between 14°C and 18°C. The authors developed a classification scheme to describe the wide variability of the bubble plumes. Bubble size distributions were measured for the various plume types and void fractions from 0.2% to 2.3% were obtained [*Leifer and de Leeuw*, 2006, Table 3]. Characteristics such as plume formation rate, plume life cycle, and plume penetration depth scaled with the wave characteristics (e.g., wave height) were presented for the various plume types [*Leifer et al.*, 2006]. The plume formation rate was strongly dependent on fetch.

[19] *Blenkinsopp and Chaplin* [2007] and *Rojas and Loewen* [2010] both utilized a fiber optic probe to investigate the temporal and spatial variations of void fraction in bubble clouds and splashes formed by mechanically generated breaking waves. Peak void fractions up to 96–99% were reported immediately after breaking.

2.4. Breaking Waves

[20] Characteristics of bubbles, bubble clouds, and whitecaps are linked to the characteristics of wavefield and breaking waves. Significant efforts were expended on formulating and observing criteria for breaking waves [*Massel*, 2007; *Babanin*, 2009]. According to the geometric wave breaking criterion, breaking occurs when the steepness parameter ak reaches its limit of 0.443 [*Babanin*, 2009, p. 342], where a is the wave amplitude, half of the wave height $a = H/2$, and k is the wave number. This limiting value arises from the Stokes limiting steepness $(ak)_{\mathrm{lim}} = \pi H/\lambda$, where λ is the limiting wavelength. The Stokes limiting wave height transforms to $H \geq 0.027gT^2$ when presented in terms of wave period via the deep water dispersion relationship [*Massel*, 2007, p.14]. This limit decreases to $H \geq 0.020gT^2$ for an irregular wavefield having broadband spectrum and involving incipient breaking waves [*Ochi and Tsai*, 1983]. A wave breaking parameter $H/(gT^2)$ obtained from this limit is often used to evaluate the conditions under which observed waves break. Statistical analysis of a large set of independent laboratory and field data for wave steepness revealed a limit much higher than this modified Stokes limit due to the asymmetry of the breaking wave profile, values for ak of 0.55 for the front wave face and of 0.44 for the rear side of the wave were reported [*Toffoli et al.*, 2010]. *Babanin* [2009] studied the asymmetry of the breaking wave profiles [see also *Bonmarin*, 1989] and the various breaking criteria. He suggests that modulational instability is the factor responsible for the breaking of dominant waves, i.e., waves break when they reach a steepness at which they become unstable, but the mechanism by which the waves grow to this limiting steepness (wind or mechanical wave maker) is not a determining factor.

2.5. Photographic Measurements of Bubble Clouds

[21] The photographic technique provides data on both the dimensions and the void fraction of bubble clouds. Key is the illumination scheme that best visualizes the bubble clouds. To obtain the void fraction of the bubble cloud, it is necessary to distinguish the air content in the air-water mixture of the clouds. Intensity threshold can be used for such a distinction.

[22] There are three main illumination schemes—back, front, and side lighting. In back lighting, the light source is behind the object and points directly toward the camera. *Leifer et al.*'s [2003a, Figure 1] system for measuring large bubbles uses backlighting and observes the bubbles as "dark rings with bright interior" [*Leifer et al.*, 2003a, Figure 12]. In front lighting, the light source is on the same side as the camera relative to the object illuminating a sampling volume in front of the camera [*Stokes and Deane*, 1999; *Leifer et al.*, 2003a, Figure 3]. In the front lighting configuration, large

Table 1. Wave Characteristics for Different Wind Speeds

Wind Speed U (m s^{-1})	Peak Frequency f (Hz)	Peak Frequency SD σ_f (Hz)	Period T (s)	Wave Length L (m)	Phase Speed c (m s^{-1})	Significant Wave Height H_s (cm)	Parameter $\frac{H_s}{gT^2}$	Breaking Steepness ak	Orbital Velocity u_d (cm s^{-1})	Wave E_p = E_k (J m^{-2})
9	1.67	0.14	0.598	0.558	0.933	6.04	0.0172	0.340	31.73	1.12
10	1.62	0.13	0.616	0.593	0.962	7.01	0.0189	0.371	35.73	1.50
11	1.60	0.12	0.625	0.609	0.975	7.80	0.0204	0.402	39.21	1.86
12	1.47	0.11	0.682	0.725	1.064	9.12	0.0200	0.395	42.02	2.54
13	1.50	0.12	0.667	0.693	1.040	9.54	0.0219	0.432	44.96	2.78
14	1.43	0.069	0.698	0.759	1.088	10.62	0.0220	0.440	47.82	3.45
15	1.38	0.07	0.723	0.815	1.128	10.89	0.0213	0.420	47.33	3.63
16	1.34	0.085	0.747	0.870	1.165	11.39	0.0208	0.411	47.91	3.97

bubbles appear as bright rings, while small bubbles appear as bright spots [see *Stokes and Deane*, 1999, Figure 7]. In side lighting, the light source and the camera are at an angle relative to each other, e.g., 45° or 90°, and thus illuminate and view the bubbles from different angles. The "overview camera" in the *Leifer et al.* [2003a, Figure 1] system is an example; the bubbles appear as bright spots in this configuration [see *Leifer et al.*, 2006, Figure 1].

[23] Various approaches have been used to obtain bubble sizes from images [*Walsh and Mulhearn*, 1987; *Stokes and Deane*, 1999; *Leifer et al.*, 2003b]. Some of these approaches require the bright spots or rings of the bubbles to be distinguished from the surrounding scene [*Stokes and Deane*, 1999; *Leifer et al.*, 2003b]. Typically, intensity threshold is used to perform such distinction. *Leifer et al.* [2003b] describe a procedure for determining the intensity threshold and sizing the bubbles. The extraction of whitecap fraction from photographs has also used this intensity threshold approach [*Nordberg et al.*, 1971; *Monahan*, 1993; *Kraan et al.*, 1996; *Asher and Wanninkhof*, 1998]. *Stramska and Petelski* [2003] determined an intensity threshold by finding an intensity level which ensured that the geometry of the whitecaps in the original gray scale images was comparable to that in the images with pixels above the threshold. Intensity variations around this threshold caused little variations in estimates of the whitecap fraction. *Sugihara et al.* [2007] quantified this approach by estimating the whitecap fraction for all intensity levels in a gray scale image (from 0 to 255) and identified as optimal the threshold for which a change in intensity by ± 6% resulted in a relative change of whitecap fraction by 10–20%.

3. Experiment

3.1. Equipment

[24] The experiments on bubble cloud characteristics were performed in the 42 m long wind-wave tank of the Air-Sea Interaction Laboratory at the University of Delaware in June 1996 and January 1997. The tank is filled to a depth of 0.75 m with filtered tap water to prevent corrosion of the supporting instruments. The height of the air column above the water is 0.55 m. The width of the wind-wave tank is 1 m, and the effective length is 37 m. A fan produces wind speeds up to 16 m s^{-1}. The wind velocity was monitored with a Pitot tube.

[25] Powerful lamps of 500 W and 600 W illuminated the formation of bubble clouds. A standard video camera recorded bubble clouds at 30 frames per second (fps). The camera used a lens with focal length of 12.5 mm and an aperture of 5.6. The depth of field with these camera settings allowed everything along the width of the wind-wave tank to be in focus. A shutter speed of 1 ms effectively froze the cloud. The video records were subsequently digitized with a frame grabber controlled by interactive imaging software.

[26] The surface elevation was registered in 3 min records with a capacitance wave gauge. The sensor was calibrated at the beginning and at the end of each experiment. The output of the wave gauge was digitized by a 12-bit analog digital converter set to a dynamic range of ±10 V and sampling frequency of 100 Hz.

3.2. Experimental Conditions

[27] Video records of the bubble clouds were taken 26 m downwind from the fan. Wind speeds were varied from 9 to 16 m s^{-1} (see Table 1). Images of bubble clouds were recorded for 15 min for each wind speed in either side or top view.

[28] Various lighting schemes were tried to visualize the bubble clouds. Backlighting with lamps positioned behind the back wall of the tank and toward the camera produced dark silhouettes of the bubble clouds. A drawback of this configuration was that bubble clouds which formed both in the center of the tank and on the tank walls were dark and could not be distinguished from one another (see also section 4.1). Front lighting with lamps located next to the camera toward the front wall of the tank made the bubble clouds bright. However, to avoid reflections from the front tank wall, the lamps had to be placed much higher than the camera.

[29] For each camera view, optimal illumination was obtained by locating the lamps in a side lighting scheme—the lamps are orthogonal to the camera plane of view. For example, in a side view, a lamp shines from above through an opening in the tank cover and illuminates a long and relatively narrow section of the water body (120 cm × 70 cm) in the center of the wind-wave tank; a black screen was placed on the back wall of the tank. In a top view, the scene was illuminated with a lamp located next to the sidewall of the tank and lower than the water surface to minimize reflections from the water surface. For both camera views, the contrast was improved by turning off all ambient lighting. The overall result is that the bubble clouds are the brightest objects in both side and top camera views.

4. Data Processing and Analysis

4.1. Images for Analysis

[30] Figures 1a and 1c show bubble clouds in side and top views that are suitable for analysis. Figures 1b and 1d depict

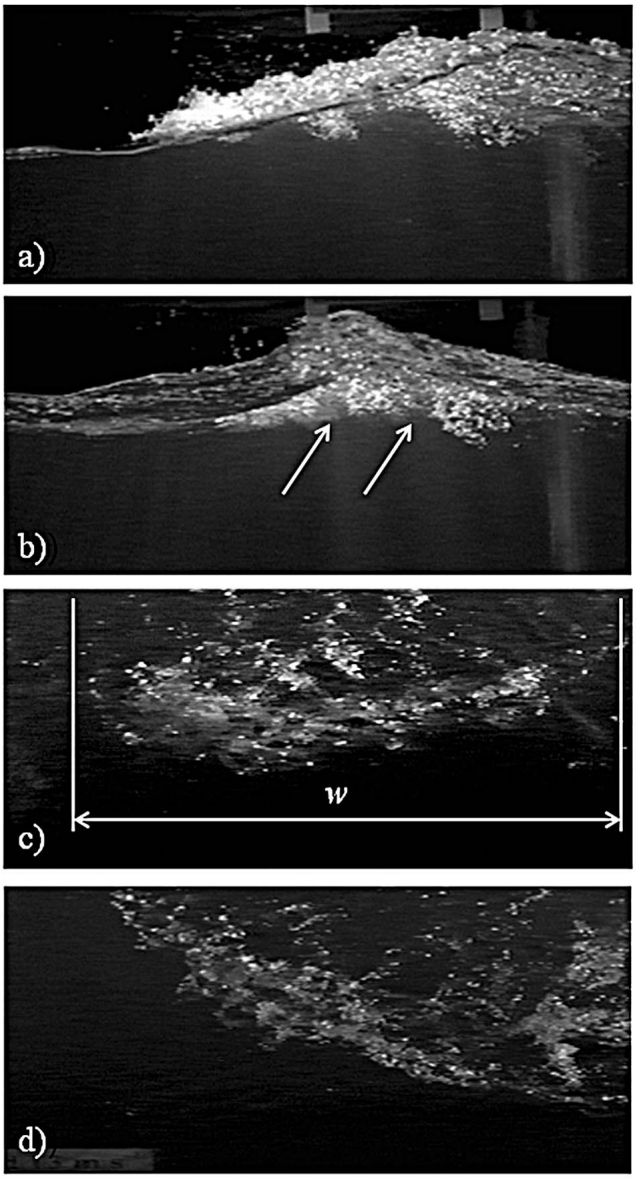

Figure 1. Choice of an image for analysis; examples of (a) cloud suitable for digitizing and further analysis in side view, (b) low meniscus on the front wall of the tank and overlapping of a cloud formed in the middle of the channel by plumes formed on the tank wall (gray patches over the bright cloud marked with arrows), (c) cloud suitable for digitizing and extraction of the cloud width (w) in top view, and (d) top view of a cloud advected from right.

images deemed unsuitable for analysis due to various problems. One problem is associated with the waterlines (meniscuses) on the sidewalls of the tank (Figure 1b). The upper part of the bubble clouds in the middle of the tank is obscured if the water line on the front wall is lower than that on the back wall. The arrows in Figure 1b point to another problem associated with bubble clouds formed in the vicinity of the boundary layers of the sidewalls of the wind-wave tank. These boundary layer bubble clouds obscure the bubble clouds in the illuminated section in the center of the tank. But they were easily distinguished from those in the middle of the tank as they are outside of the central illuminated section and hence darker. *Longuet-Higgins* [1990] showed that the waves near the wall might be significantly steeper than those along the centerline. Hence, they may break and produce bubble clouds even when the wave in the middle of the tank do not break. Images with such boundary layer bubble clouds were not analyzed. Figure 1d shows a problem associated with top view images. Here the bubble cloud is being advected from right to the left of the image. Images with such bubble cloud motion were not selected for analysis because the width of the bubble cloud cannot be well defined.

[31] The intensity level varied from 0 (black) to 255 (white) in the gray scale images (Figure 1a). To better control intensity variations in the background of the bubble clouds, the illuminated scene without bubble clouds was recorded before each experiment. Figure 2a shows the background lighting for the side view: the illuminated water body is gray

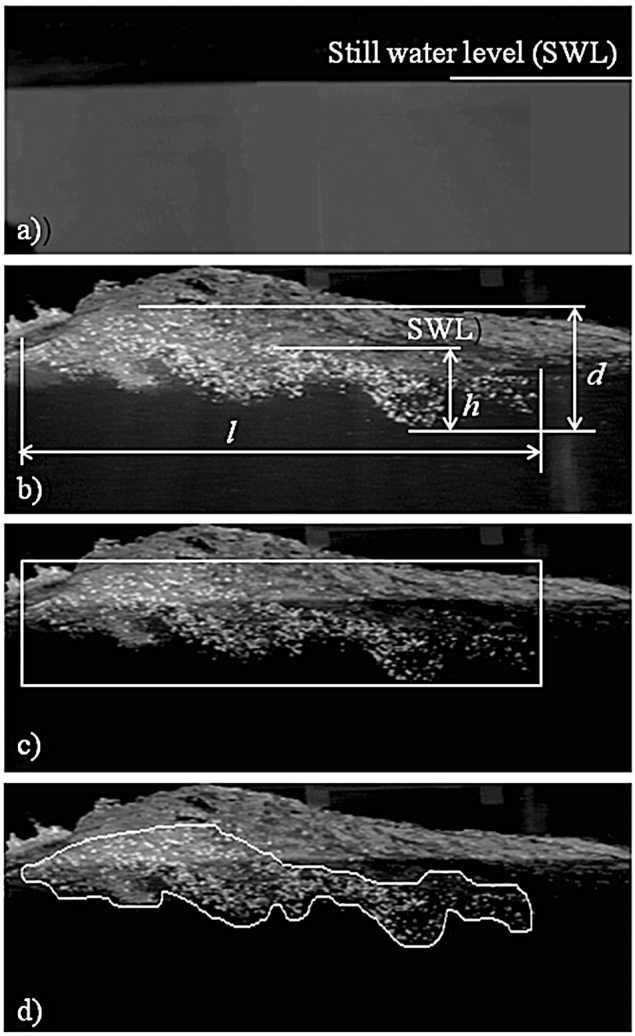

Figure 2. Definition and procedure for extraction of the bubble cloud characteristics: (a) background field of view (FOV) and (b) characteristics observed from side view: length (l), thickness (d), and penetration depth (h). (c) Rectangle window for determining l, d, h cloud. (d) Cloud cross section.

(about 10 intensity units (IU)), while the air column above is almost black (2 to 5 IU). The two intensity levels are uniform across the images. Subtracting this image from raw images of the bubble clouds (seen in Figure 2b) improved the contrast between the clouds and the background (Figure 2c). The images thus prepared for analysis had background intensity level of about 2 IU.

4.2. Extraction of Bubble Cloud Characteristics

[32] The length, thickness, and penetration depth of the bubble cloud were extracted from the side view images. Figure 2b illustrates our definition of these cloud dimensions. The bubble cloud length l is defined as the distance between the vertical lines passing through the left and right edges of the cloud. The bubble cloud thickness d is defined as the distance from the highest to the lowest edges of the cloud. The distance from the SWL to the lowest point is defined as the penetration depth h of the bubble cloud. The width w of the bubble cloud is extracted from top view images as the distance from the left-most to the right-most edges as shown in Figure 1c. The values of l, d, and h were determined using a rectangular window circumscribed around the cloud (Figure 2c) and the SWL obtained from the background images (Figure 2a).

[33] Optimization of the lighting and background intensity of the images (sections 3.2 and 4.1) results in bubbles and bubble clouds being the brightest objects in the images. The white line in Figure 2d delineates the cross section of the bubble cloud A_t. It is irregular in shape and can be traced with the image software. Two rules were observed to establish repeatability in determining cloud cross sections: 1) the cloud is represented by the brightest pixels; and 2) bubble clouds comprise more than a minimum number of bubbles, arbitrarily chosen to be 5. Following these rules, the bubble cloud cross section can be framed with 99% repeatability. In an image with horizontal and vertical resolutions of Δx and Δy, respectively, the cloud cross section is $A_t = N\Delta x\Delta y$, where N is the total number of pixels within the irregular area of air-water mixture A_t. Air bubbles occupy an area $A_a = N_a\Delta x\Delta y$, where N_a is the number of bright pixels, representing the air bubbles within A_t.

[34] Void fraction is defined as the ratio $\alpha = V_a/V_t$ of the volume occupied by the air bubbles V_a in a volume of air/water mixture V_t. For the bubble clouds in our configuration $V_t = A_t.b$ and $V_a = A_a.b$, where $b = 70$ cm is the width of the illuminated section in the middle of the tank (section 3.2). Often a thin sheet of light (e.g., a laser sheet) is used to make "local" estimates of the void fraction. These estimates will vary across the width of the tank, and so an average void ratio will have to be calculated in order to give a representative value for the whole cloud. In our approach, the side view images (Figure 2d) represent a laterally integrated view of the cloud over width b. This is effectively an ensemble of thin vertical planes of illumination. Therefore, the void ratio is independent of the thickness of the light sheet. This allows us approximate evaluation of the void fraction of the bubble cloud.

[35] Once the irregular cross section of the cloud was delineated, two counts were made within it: one count of all pixels to obtain N and second count of pixels with intensity above 10 IU to obtain N_a. The intensity threshold was chosen in a manner similar to that of *Stramska and Petelski* [2003]. That is, we changed the intensity to 5, 10, 20, and 30 IU noting the threshold for which the changes of the bubble cloud geometry was minimal compared to that in the original images. Empirically, we determined that a threshold of 10 IU fulfilled this requirement, and was low enough to count even faint pixels representing the very small bubbles or those deep in the water volume. On some occasions this threshold was not high enough to reject the intensity of the wave lying behind the cloud; Figure 2d show such a case. Therefore, some overestimation of the bright pixels number occurred. However, since the cloud/wave overlying areas were usually smaller than the remaining cloud area, this overestimation introduced an error of less than 5%.

[36] For the kinematics of the bubble cloud (section 5.3), we tracked, from image to image, the center of mass of one plume within a bubble cloud at wind speed of 13 m s^{-1}. The extracted time series of the horizontal and vertical positions $x(t)$ and $z(t)$ of this point were used to obtain the velocities of the bubble cloud in the tank.

4.3. Data Spatial Resolution and Time Series

[37] In its standard mode, the frame grabber used to digitize the video records captured 11 interlaced images of 752 × 480 pixels at a time before transferring them to the computer. At a rate of 30 fps, this provided a sequence of images for a time span of 367 ms. Such a time period would not be enough to register a bubble cloud from its appearance to its decay. Keeping the same time step of 1/30 s, we increased the time span to 767 ms by using non-interlaced mode, i.e., a field of 752 × 240 pixels instead of a frame was captured. We achieved an even longer time interval by cropping and digitizing a window from the full field of view (FOV) of the camera.

[38] For the side view records, the FOV of the camera in horizontal and vertical directions was 77 cm × 62 cm; the horizontal and vertical resolutions are $\Delta x = 1$ mm pxl^{-1} and $\Delta y = 2.5$ mm pxl^{-1}. A cropped window 67.2 cm wide and 37.5 cm high was digitized. This allowed sequences of up to 41 images to be captured, which in all cases was more than enough to register the entire lifetime of the cloud. The wavelength of the dominant wave (section 4.5 and Table 1) and the physical size of the digitized window (67.2 cm) were used to estimate what portion of the wave profile at a given wind speed fits in. The 67.2 cm width accommodated the entire wavelength for lower wind speeds (9–11 m s^{-1}) and about 80% of the wavelength for higher wind speeds (12–16 m s^{-1}).

[39] For the top view records, the camera FOV on the water surface was 79 cm across the tank and 58 cm along the tank with respective resolutions of 1.03 mm pxl^{-1} and 2.4 mm pxl^{-1}. A window of 69 cm across and 57 cm along the tank was digitized. This allowed the bubble cloud width w to be traced from its appearance to its almost complete decay in sequences of up to 26 images.

[40] A sequence of images represented the time evolution (or lifetime) of a bubble cloud. The first image in which a bubble cloud is observed is set at $t_0 = 0$. Each consecutive image is at time step $\Delta t = 1/30$ s (≈33 ms). The bubble cloud characteristics were extracted from the consecutive images forming time series for the evolution of each characteristic during a bubble cloud event. Figure 3a consists of plots of 10 time series for bubble cloud length l (thin lines), and

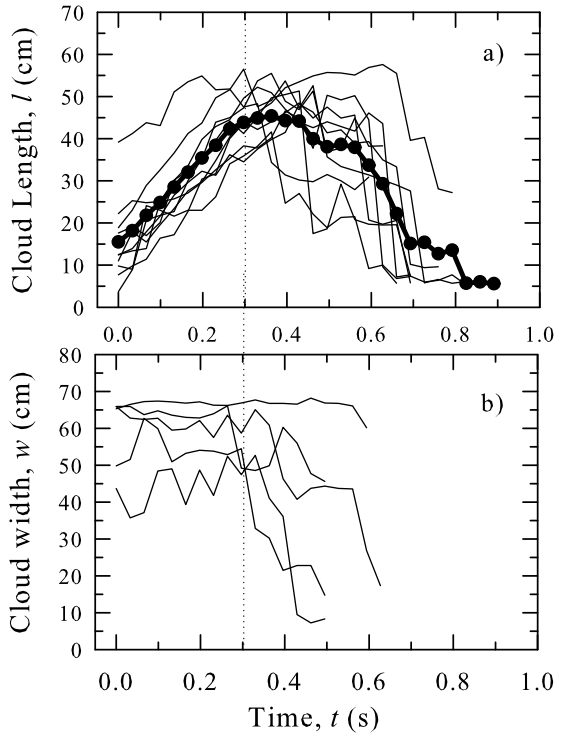

Figure 3. Time series of bubble cloud characteristics for wind speed of 13 m s^{-1}: (a) 10 time series for bubble cloud length l from side view (thin lines; thick line with symbols shows ensemble averages at time steps of 1/30 s) and (b) 5 time series for bubble cloud width w from top view.

Figure 3b consists of plots of 5 time series for bubble cloud width w, at wind speed of 13 m s^{-1}. The variability of bubble cloud characteristics (l, w, and lifetime) for a given wind speed is evident in Figure 3. The variability is further discussed in sections 5.4 and 5.5.

4.4. Bubble Cloud Statistics

[41] The evolution of bubble clouds is inherently nonstationary and spatially variable. Statistical approaches are thus required to quantify bubble cloud characteristics, including probability density functions (PDFs). Physically, various factors determine the nonstationarity of the bubble clouds. Wave breaking phenomena are intermittent and time varying; the bubble clouds appear, grow, and decay; the bubbles within the clouds rise, dissolve, and coalesce, etc (section 1). Figure 3a illustrates that the ensemble mean values for the 10 time series of bubble cloud length l are nonstationary.

[42] We use ensemble averaging to analyze the nonstationary bubble cloud data. For this purpose, we sort the available data into groups which ensure quasi-stationarity. Usually the bases for such grouping of the data are the various underlying physical processes which bring about the observed nonstationarity. Thus, to process our data with ensemble averaging, values for bubble cloud characteristics from 5 or 10 time series, such as those shown in Figure 3, were grouped by two criteria. The first criterion used the temporal evolution of each of bubble cloud characteristics; the second criterion considered the association of the bubble cloud characteristics with specific wave phase. On the basis of the temporal evolutions, we separated the data into "growth" and "decay" stages. These stages, denoting the short-lived and long-lasting features of the bubble clouds, are analogous to the α- and β-plumes defined by *Monahan and Lu* [1990]. The former describes data for times $t \leq 0.3$ s (Figure 3), the latter refers to the values for times $t > 0.3$ s. For the grouping of the data by wave phase, the images in each sequence were visually examined and separated in six groups, each covering 45° and assigned $\varphi = 45°$, 90°, 135°, 180°, 225°, and 270°. Usually 2–3, occasionally 5, cloud images from one sequence fell in one "phase" group. Mean values and standard deviations were evaluated for each temporal stage and phase group.

[43] For the PDFs, the values of a given bubble cloud characteristic in a temporal stage, growth or decay, were divided in 12 bins and the resulting histograms were normalized with the total number of data points and the respective bin width.

4.5. Wavefield Characteristics

[44] The wavefield characteristics were determined in order to scale (non-dimensionalize) the bubble cloud characteristics. The 3 min time series of surface elevation (section 3.1) were divided into 18 shorter ones, each of 1000 points. Power spectra were calculated for each series. The peak frequency f (Hz) of each power spectrum was found, and then the 18 peak frequencies were averaged and reported (with their standard deviations (SDs)) as the dominant wave frequencies for each wind speed (Table 1). The time series were also used to find the significant wave height H_s as the average of the one third highest wave amplitudes.

[45] The frequency peak was used to find the dominant wave period T (s). The wavelength L was calculated from the dispersion relation $\omega^2 = gk.\tanh(kD)$, where $k = 2\pi/L$ is the wave number, $\omega = 2\pi/T$ is the angular frequency, D is water depth, and g is the acceleration due to gravity. The phase velocity is $c = L/T$.

[46] We used the characteristics of the dominant wave (k and ω) to represent the time series of the bubble cloud positions $x(t)$ and $z(t)$ (section 4.2) relative to the wave phase using the phase function $\varphi = kx - \omega t$. Because this expression transforms to $\varphi = k(x - ct) = kx'$, the representation of the bubble cloud data as a function of $\varphi(x, t)$ is equivalent to an observation from a frame of reference moving with the phase velocity of the dominant wave.

5. Results

5.1. Wavefield During Experiments

[47] For our experimental setup, the wind-generated waves were deep water waves as half of the wavelength L is less than water depth D. We observed $D/L > 0.8$ for all wind speeds (section 3.1 and Table 1).

[48] The averaged power spectra of the water surface for wind speeds of 10, 12, 14, and 16 m s^{-1} are plotted in Figure 4a. Two trends are evident. First, the spectral densities increase as the wind speed increases. Second, the spectral peak shifts toward lower frequencies. Similar results were reported by *Mitsuyasu and Honda* [1974]. Figure 4b shows that in the equilibrium range, which spans frequencies above twice that of the spectral peak (frequencies above ≥1.5 Hz), the spectra have slopes close to f^{-4} as predicted by theory [*Phillips*, 1985] and observed in the ocean

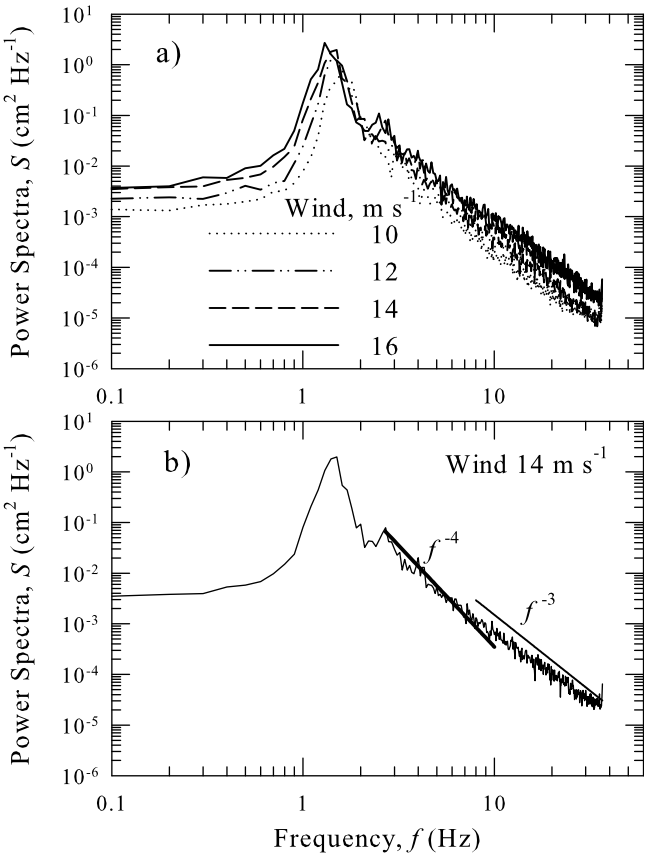

Figure 4. Power spectra of surface elevation: (a) wind speeds of 10, 12, 14, and 16 m s^{-1} and (b) spectrum for 14 m s^{-1} with slopes of f^{-4} and f^{-3} in the equilibrium range.

[*Mitsuyasu*, 1977; *Forristall*, 1981]. For frequencies above 8 Hz, the slope transitions to f^{-3} because of Doppler shifting [*Phillips*, 1985; *Banner et al.*, 1989].

[49] We consider wave breaking criteria (section 2.4) in order to compare our experimental conditions to wave breaking generated by mechanisms other than wind. The wave breaking parameter $H_s/(gT^2)$ for the conditions during our experiments is evaluated using the wavefield measurements (section 4.5). Values of $H_s/(gT^2)$ ranged from 0.017 to 0.022 (Table 1). These values are consistent with previous measurements in the same wind-wave facility [*Xu et al.*, 1986] and comparable to those previously reported for mechanically and wind-generated waves [*Griffin et al.*, 1996]. Figure 5 shows that values of $H_s/(gT^2)$ for the wind-generated wavefield in the tank are in good agreement with the modified Stokes limit (black line). For reference, the Stokes limit for a (regular) wavefield with a narrow-band spectrum is given as a gray line. This result lends support to *Babanin*'s [2009] argument that the wave steepness is the determining factor for the wave breaking (section 2.4). In terms of steepness criterion, the wave steepness values $ak = \pi H_s/L$ range from 0.34 to 0.44 in our experiment (Table 1). These values are in accord with results of *Toffoli et al.* [2010].

[50] Orbital motion associated with the dominant waves, defined as $u_d = a\omega = \pi H_s/T$, ranges from 32 cm s^{-1} to 48 cm s^{-1} depending on the wind speed (Table 1). These values are 34% to 41% of the phase speed c and could modulate the velocity field of the flow. *Melville* [1983] and *Gemmrich et al.* [2008] point out that the local characteristics of the breaking wavefield rather than those of the dominant wave are more appropriate to evaluate the velocity modulation of highly localized bubble cloud events. We do not correct our bubble cloud data for orbital motions of the wavefield because we do not have enough information to determine the local wave characteristics associated with each cloud event.

5.2. Bubble Cloud Description

[51] The number of bubble clouds N_c produced for different wind speeds (9–16 m s^{-1}) and in different time intervals t_{obs} (1, 3, 5, 10, 15 min) were counted from the video records. The number of events increases with wind speed and time interval. For example, Figure 6a shows that for t_{obs} = 10 min (inverted triangles) about one hundred events occur at 10 m s^{-1} wind and more than 300 at 16 m s^{-1}. The production rate P, defined as the number of events per unit time interval N_c/t_{obs}, increases steadily with increasing wind (Figure 6b). The production rates collapse well and do not depend on t_{obs}, except for t_{obs} = 1 min. The approximate collapse for different time intervals is to be expected when the ratio of observational period t_{obs} to the wave period T is large (i.e., $t_{obs}/T \gg 1$). The data for t_{obs} = 1 min do not fully collapse. This suggests that there are significant dynamics on time scales of about 1 min, which is much longer than the wave period (typically less than 1 s, see Table 1). That a 1 min averaging period is not sufficiently long to collapse the data indicates that the effects of bubble plumes persist beyond one wave period. This is in agreement with findings of previous measurements that "a dissipative layer," in which energy lost by breaking waves generates currents, vorticity, and turbulent mixing, persists for $O(100)$ wave periods [*Rapp and Melville*, 1990; *Melville*, 1994].

[52] Typical images of bubble clouds from side and top views at several wind speeds are shown in Figures 7a and 7b. It is evident that the clouds become longer, thicker, and wider, penetrate deeper, and contain more air with increasing the wind speed. The deepening with increased wind speed of the bubble clouds seen here is consistent with the deepening

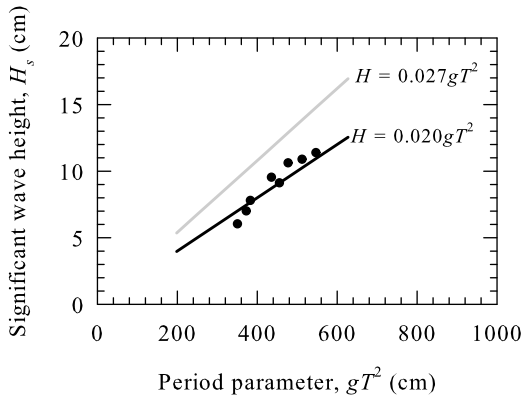

Figure 5. Measured significant wave height H_s as a function of period parameter gT^2 together with the limiting steepness for irregular waves (black line); the limiting steepness for regular waves (Stokes's limit) is shown with gray line for reference.

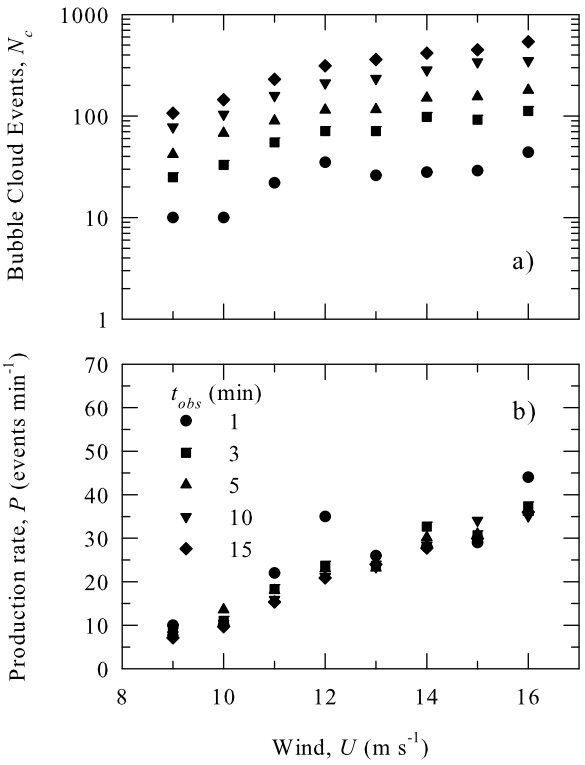

Figure 6. Bubble cloud production N_c as a function of wind speed U: (a) number of the events for different observing time intervals t_{obs} and (b) bubble cloud production N_c normalized by the observing time interval t_{obs}. The legend of symbols applies to both figures.

of the bubble plume scale depth with wind speed discussed by *Thorpe* [1982].

[53] The time evolution of a bubble cloud is shown in Figures 8a (side view) and 8b (top view) with a sequence of images at time intervals of Δt = 167 ms and Δt = 100 ms, respectively. The evolution of the bubble cloud in Figure 8a is typical. The bubble cloud evolves through several descending, approximately circular plumes. These circular plumes sometimes rotate. Each of these plumes, and the cloud as a whole, grows quickly, reaches some maximum size and then decays on a time scale less than one wave period (section 5.4). In Figure 8a, the images at times of 0, 167 ms and 334 ms visualize the bubble cloud evolution in the growth stage, which occurs up to about 300 ms (see Figure 3). The images at times of 501 ms and 668 ms are in the decay stage (also see Figure 3); the signature of the subsequent or following breaking wave and bubble cloud is also evident at the right-hand edge of these images. The image at 334 ms shows a mixture of both growing and decaying plumes within one bubble cloud. The images at 0 and 167 ms are cases associated with phase group of 45°; the image at 334 ms is in 90°-phase group; the last two images are in 225° and 270° phase groups (section 4.4).

[54] The circular, descending plumes seen in side view look different from the top view sequence (Figure 8b). In the top view, these plumes are observed on the surface as circular patches adjacent to windy or bendy streaks of bubbles which are distributed across the cloud width. The semi-circular or bow-like form of the cloud at early times (e.g., moment t_0 in Figure 8b) disintegrates quickly into such streaks. For example, streaks are already evident by 100 ms in Figure 8b, a time scale comparable to that *Deane and Stokes* [1999] observed in the field for disintegration of dense bubble population to individual bubbles (section 2.2). The observed streaks are similar to features documented in the literature. *Bondur and Sharkov* [1982] analyzed aerial photographs and reported areal values of short-lived foam patches, which they called "dynamic" foam, associated with the instant of wave breaking and more durable "static" foam that follows the breaking event. *Bortkovskii* [1987] also distinguishes initial bright "whitecaps" and "foam bands" left after the wave passage.

[55] Observations showed that the position of the bubble cloud inception on the front face of the wave changes with the wind speed. The initial air entrainment is mostly around $\varphi = 45°$ for wind of 10 m s^{-1}, and around $\varphi = 33°$ for 16 m s^{-1} wind. These values concur with *Koga*'s [1982] qualitative description.

5.3. Bubble Cloud Kinematics

[56] We now describe the kinematics of the centroid of the bubble cloud by discussing its horizontal and vertical positions $x(t)$ and $z(t)$ and horizontal and vertical velocity components $V_x(t)$ and $V_z(t)$. In a frame of reference (FoR) fixed with the observer and oriented along the wind direction (x is positive from right to left) and down into the water (z is positive downward), the positions of one cloud created under 13 m s^{-1}-wind in the tank are given in Figure 9a. We describe the trajectory of the cloud in terms of times t_0 (inception) to t_c. The cloud travels forward and downward (until t_1), then it moves upward until t_2, and finally lingers in almost one place until the end of its lifetime at $t_c \sim 0.7$ s. This is consistent with the motionless decaying plumes observed by *Bezzabotnov et al.* [1986] in the field (section 2.2).

[57] Further insight is derived by presenting the bubble cloud positions relative to the wave phase φ (see section 4.5 for the estimation of φ). Figure 9b shows the vertical positions $z(\varphi)$; the profile of a regular sinusoidal wave having characteristics T, L, and c of the dominant wave at wind speed of 13 m s^{-1} (Table 1) is shown for reference. Comparing Figures 9a and 9b, the initial deepening of the cloud (from t_0 to t_1) corresponds to the wave phase range of 45°–70°; the subsequent upward motion is associated with wave phases shortly before, at, and just behind the wave crest (70°–135°); the plume descends with the wave trough ($\varphi > 135°$).

[58] Figures 10a and 10b show the evolution of the cloud velocities along the tank V_x and in depth V_z. The plume enters the water with a horizontal speed of about 60 cm s^{-1} ($\sim 0.6c$) (Figure 10a) and a vertical speed about 8 cm s^{-1} ($<0.1c$) (Figure 10b). The horizontal speed is quickly decelerated to about 30 cm s^{-1} ($\sim 0.3c$) during the first 0.1 s. During the same period, the downward speed decreases to zero and upward motion begins. In the time range 0.1–0.3 s, the bubble cloud reaches its maximal horizontal speed (V_x = 99 cm s^{-1} = $0.95c$), then it gradually decreases, and after 0.45 s has an average value around 4 cm s^{-1} ($\ll 0.1c$) for the remainder of the evolution (Figure 10a). After 0.45 s, the horizontal speed varies widely between 50 cm s^{-1} and -60 cm s^{-1}; this variability is further discussed in section 6.1. In the same 0.1–0.3 s time frame, the cloud reaches a maximum upward velocity of about 23 cm s^{-1} $\sim 0.2c$.

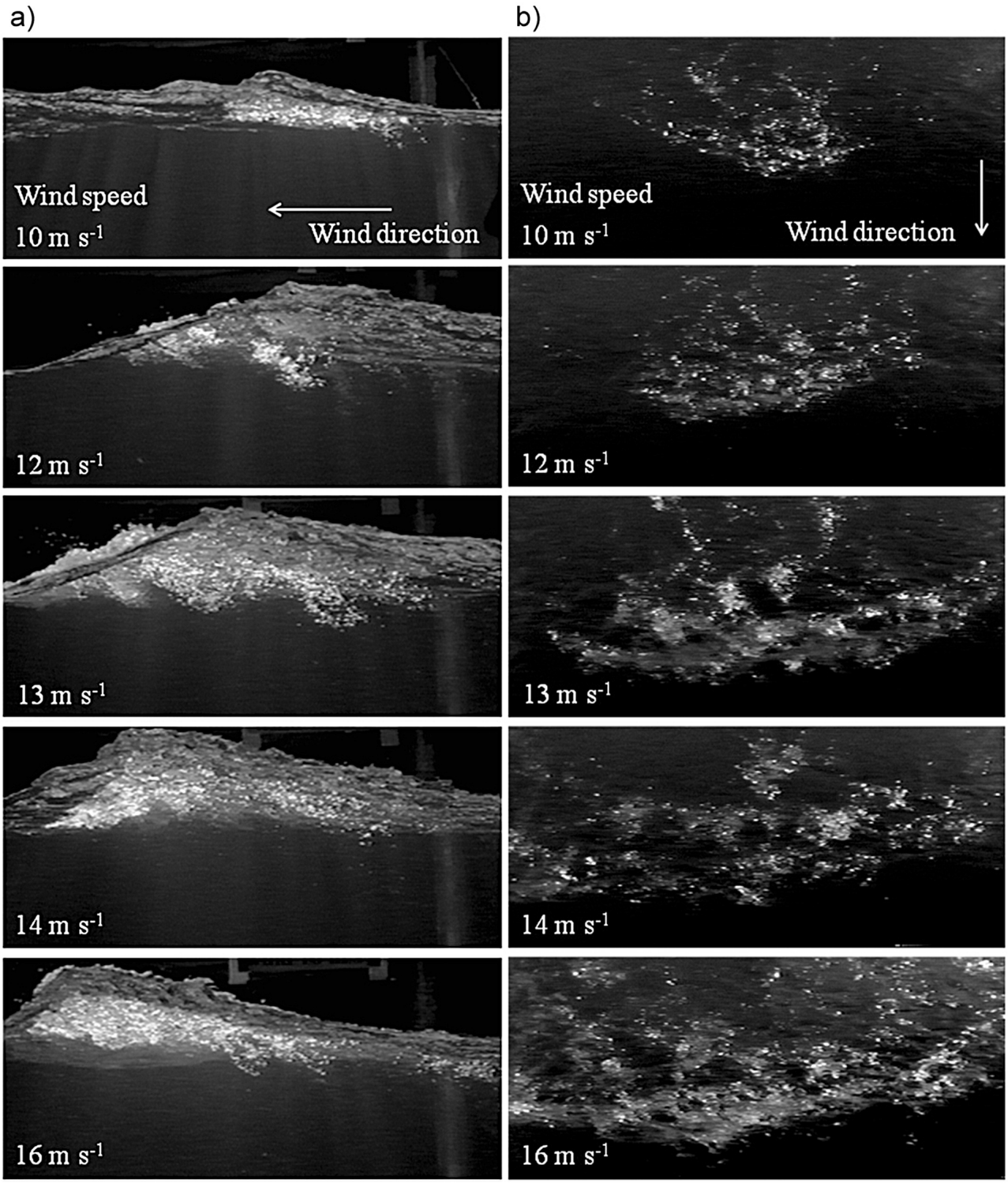

Figure 7. (a) Bubble clouds at different wind speeds in side view. In the images bubble clouds appear bright. (b) Bubble clouds at different wind speeds in top view.

Subsequently, the cloud moves generally downward with an average of 14 cm s^{-1} $\sim$ 0.1c for times after 0.45 s, with oscillations ranging from about -10 to +80 cm s^{-1}. Comparing V_x and V_z, we see that the cloud has predominantly vertical motion at the end of its lifetime ($t > 0.45$ s). At wind speed of 13 m s^{-1} the mean bubble diameter measured is 12 mm. The rise velocity for 12 mm diameter bubbles is $\sim$ 25 cm s^{-1} in pure water [*Clift et al.*, 1978, p. 172]; thus the average residual vertical motion is about 56% of the bubble rise velocity.

[59] In order to examine kinematics in terms of wave phase φ, we now consider Figures 10c and 10d which show the cloud velocities as observed from a FoR moving with the wave $V_x'(\varphi)$ and $V_z'(\varphi)$. In this FoR, the bubble cloud

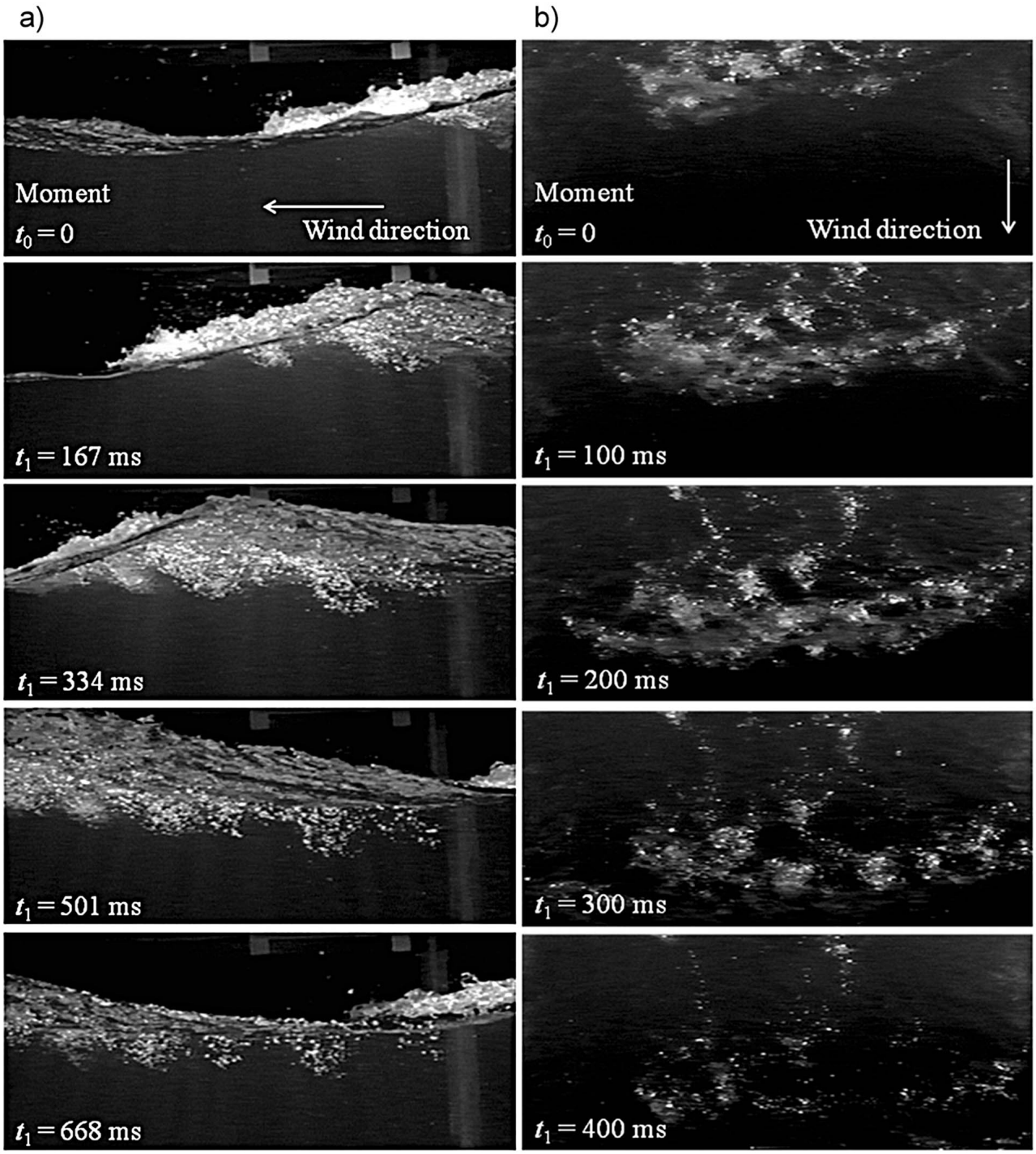

Figure 8. Bubble cloud evolution for wind speed of 13 m s^{-1}. (a) Side view, $\Delta t = 167$ ms. (b) Top view, $\Delta t = 100$ ms.

moves backward relative to the wave as $V_x' = V_x - c$. From Figure 10c, the initial horizontal deceleration is associated with the phase range 45°–75°; the increase of the cloud forward motion is related to the wave phase around the crest (70°–120°). Because for $\varphi > 120°$ the cloud is almost stationary in a fixed FoR (Figure 9a), it appears to go backward faster in the moving FoR. The upward motion of the cloud occurs for wave phase up to 120° (Figure 10d), and for $\varphi > 120°$ the cloud moves downward quickly.

[60] Further insight on kinematics arises from consideration of the scaled velocities. Figure 11a shows nondimensional cloud velocities V_x/c and V_z/c relative to the wave phase φ. The values of the ratio $|V_x/c|$ are mostly less than 0.6, occasionally approaching 1. This is in accord with *Kennedy and Snyder* [1983], *Lamarre and Melville* [1992], and *Stansell and MacFarlane* [2002] who report values for this ratio from 0.5 to 1. Values of the squared ratios $(V_x/c)^2$

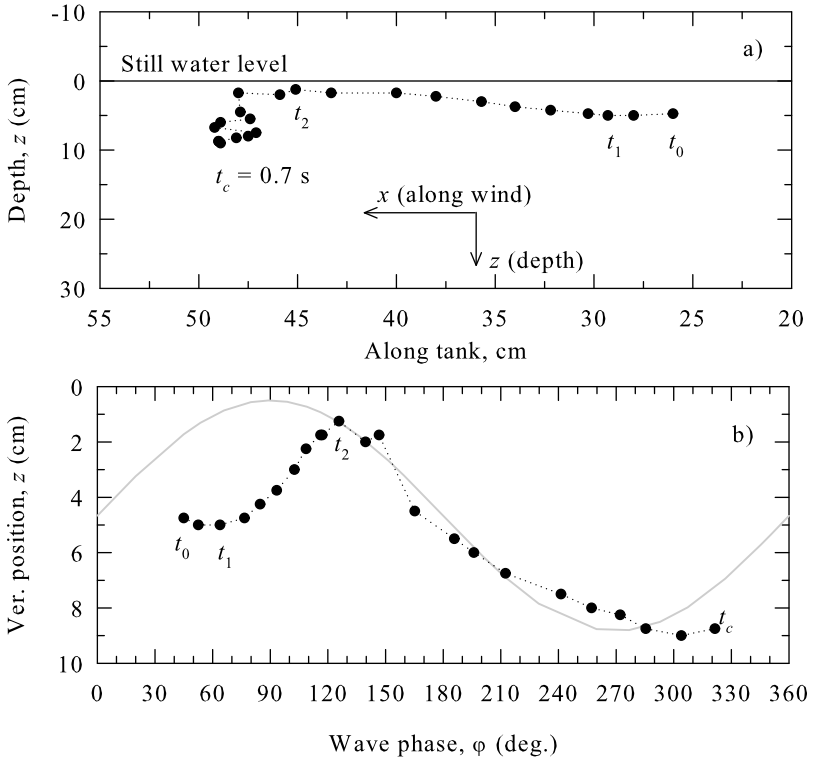

Figure 9. Horizontal and vertical trajectories of a bubble cloud at a wind speed of 13 m s^{-1}. (a) Dots show the progress of the centroid of one bubble plume along the tank in a frame of reference fixed with the observer. Axis x is along the wind speed, positive from right to left; axis z is positive downward. Times t_0 to t_c = 0.7 s mark the evolution of the horizontal trajectory. (b) Dots show the vertical trajectory relative to the wave phase φ in a frame of reference moving with the phase speed of the dominant wave (Table 1). The gray line is the profile of a regular sinusoidal wave. Note that in Figure 9a values increase along the x axis from right to left, and in Figure 9b values increase along the x axis from left to right.

and $(V_z/c)^2$ are 0 to 1 with the vertical component being smaller than the horizontal component (Figure 11b).

[61] The observations of another three bubble clouds at 13 m s^{-1} wind and other winds (10 and 16 m s^{-1}) show similar trends in space, time and relative to the wave phase. The complex motion of the bubble cloud arises from the interplay between wave forcing and evolving buoyancy forcing. We interpret the non-monotonic changes relative to the wave phase φ of the cloud positions (Figure 9b) and velocities (Figures 10c and 10d) as the effect of wave forcing. Compression and stretching arise from wave forcing due to the asymmetry and skewness of the wave profile as it steepens just before breaking [*Bonmarin*, 1989; *Babanin et al.*, 2007]. We observe the signature of compression in the first third of the wave profile where for equal time increments the steps of $\Delta\varphi$ are small (average value $\Delta\varphi \sim 8°$ for $40° < \varphi < 125°$). Stretching occurs in the wave trough where $\Delta\varphi$ steps are larger (ranging from 10° to 29° for $\varphi > 125°$). We discuss the bubble cloud dynamics in section 6.2.

5.4. Variations of Bubble Cloud Characteristics

[62] The characteristics (lifetime, l, d, h, and α) of the bubble cloud varies with wind speed and for a given wind speed. Figure 3 illustrates the variability for a given wind speed of 13 m s^{-1}. The maximum values of the lifetime of the clouds are about 1 s. This is similar to the wave period (see Table 1). Thus the process of cloud formation, growth and decay occurs primarily over one wave period. The growth of the bubble cloud typically occurred over the first 0.3 s (Figure 3); this corresponds to about (0.4–0.5)T depending on the wind speed (Table 1). A fraction of the decaying bubble plumes survives beyond one wave period and persists into the next wave period (see Figure 8a, t_3 and t_4) and even beyond (Figure 6b and section 5.2).

[63] The evolution of the bubble cloud dimensions (l and d) and void fraction α with wave phase φ for wind speeds of 10, 13, and 16 m s^{-1} is presented in Figures 12a–12c. Each point represents a mean value for each 'phase' group (section 4.4). Figures 12a and 12b show that bubble cloud length l and thickness d reach their maximal values at wave phase of around 135° (corresponding to ~0.5T), then decrease over the next 135°. The maximum cloud length varies between 0.4L and 0.6L: with a value of 0.4L for lower wind speeds and 0.6L for higher wind speeds. This is consistent with the visual observation of *Bortkovskii* [1987] that the length of the foam streaks does not exceed the wavelength. Depending on the wind speed, the thickness d varies from 4.6 cm to 17 cm (corresponding to $0.7H_s$–$1.5H_s$). This is consistent with the values reported by *Koga* [1982], *Thorpe* [1982], and *Kalvoda et al.* [2003].

[64] Values of the void fraction α steadily decreases over the entire wave profile (Figure 12c). Values of α are close to unity between 0 and 90° (corresponding to ~0–0.25T, which is part of the growth stage as defined in section 4.4)

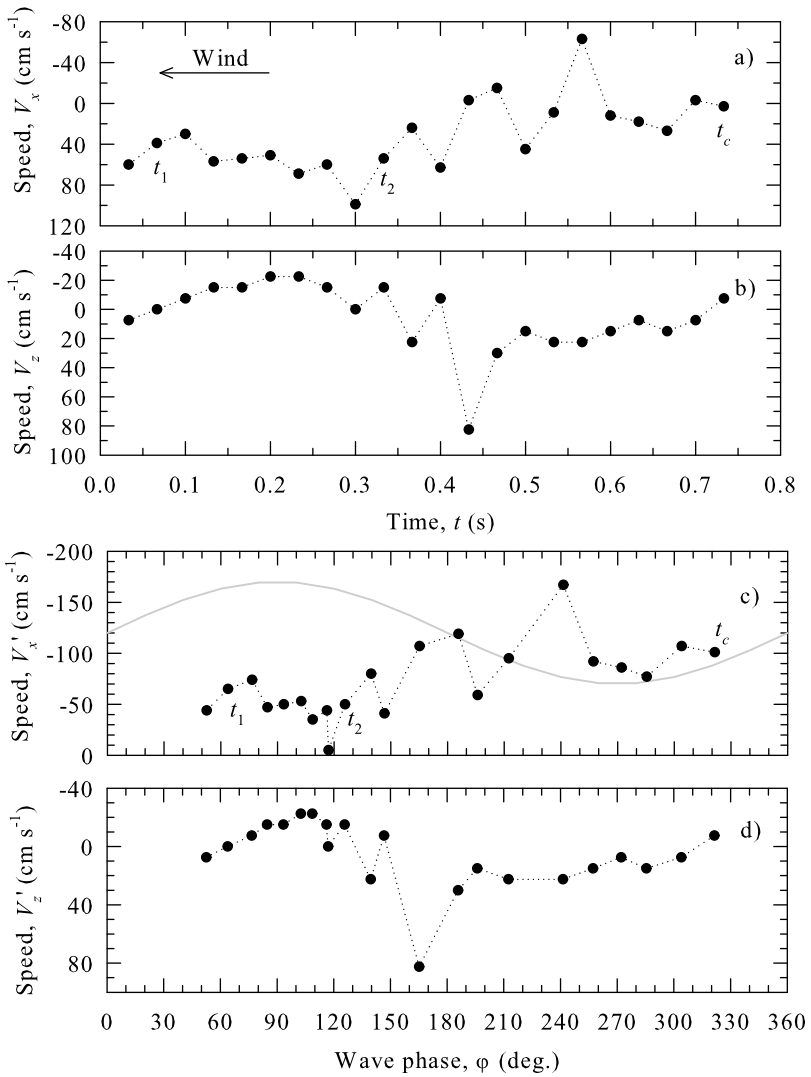

Figure 10. Speeds of the bubble cloud corresponding to the cloud positions shown in Figure 9 at wind speed 13 m s^{-1}. Dots show time evolution of cloud speeds in fixed frame of reference: (a) horizontal component V_x and (b) vertical component V_z. Dots show evolution in wave phase φ of cloud speed (moving frame of reference): (c) horizontal component V_x' and (d) vertical component V_z'. Times t_1 to t_c are the same as in Figure 9.

reflecting the initially dense bubble population. Values of α gradually decrease to 60% at about 180° (~0.7T). Depending on the wind speed, α attenuates to 20–30% at 270°. Void fraction values consistent with those reported here are documented by *Lamarre and Melville* [1991] and *Blenkinsopp and Chaplin* [2007] (section 2.3).

5.5. Statistics of Bubble Cloud Characteristics

[65] Figure 13 shows the PDFs of bubble cloud characteristics (l, d, w, and α) for wind speed of 13 m s^{-1}. Data are shown for the growth and decay stages (see section 4.4). For bubble cloud length (Figure 13a), shorter values of l (10 cm to 30 cm) are more probable during the growth stage (black line). High probability of long clouds (>30 cm) as well as very short clouds (below 10 cm) can occur during the decay stage. For the thickness d (Figure 13b), values above 6 cm to 15 cm are more probable during the growth stage, while the thinnest (<6 cm) and the thickest clouds (>15 cm) are associated with the decay stage. The shape of the PDFs for widths (Figure 13c) and void fractions (Figure 13d) differ from those of l and d. High values for w and α are much more probable during the growth stage and low values of w and α are associated predominantly with the decay stage.

[66] The effect of wind speed on the PDFs of bubble cloud thickness d is shown in Figure 14 for both growth and decay stages. For the growth stage (Figure 14a), thin clouds (up to 10 cm) are most likely for 10 m s^{-1} wind (gray line). As the wind speed increases, the range of cloud thicknesses increases and peak values shift toward thicker clouds (>10 cm for 13 ms^{-1} and > 15 cm for 16 m s^{-1}). Broadly, scaled thicknesses are $d/H_s \approx 1$ to 1.4. For decay stage (Figure 14b), the effect of increasing wind speeds is the same as for the growth stage (Figure 14a). This suggests that the effect of wind speed variations is relatively more important in determining the range of cloud thicknesses; the growth and decay stages have a secondary effect on the

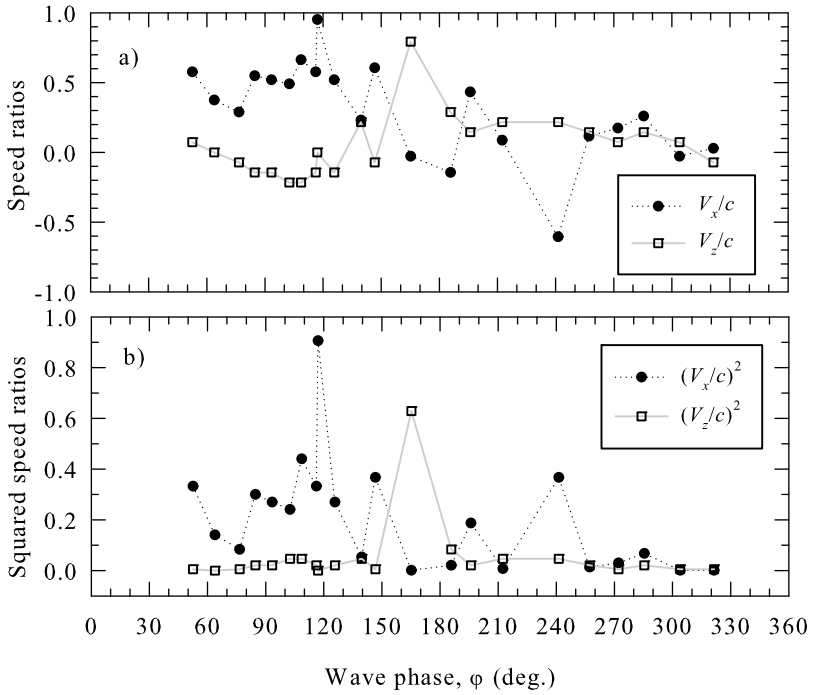

Figure 11. (a) Speed ratios V_x/c and V_z/c and (b) squared speed ratios $(V_x/c)^2$ and $(V_z/c)^2$ as a function of wave phase φ. Data for wind speed of 13 m s^{-1}.

range of cloud thicknesses. Though not shown, wind speed variations have similar effect on the PDFs of other cloud characteristics (l, w, and α).

[67] Bubble cloud statistics reveals that both temporal variations (i.e., various stages of cloud lifetime) and forcing parameters (wind speed in this experiment) lead to the high variability of the bubble cloud characteristics, their surface expression as whitecaps, and eventually the air-sea interaction processes associated with them. A range of possible values of cloud dimensions and void fractions can exist at any given moment because of the occurrence of various lifetime stages or from the occurrence of one stage at various wind speeds. This is therefore a quantitative verification of the expectation that in the open ocean at any moment there is a distribution of bubble cloud thicknesses, bubble cloud penetration depths, bubble cloud surface areas, and void fractions. Knowing this is important for developing models for the foam and bubbles in the ocean which produce sea spray and affect gas, heat and momentum exchange. To provide guidance for modeling, we fitted different distributions to the cloud PDFs. Gaussian and Rayleigh distributions did not provide a good fit to the PDFs of the cloud dimensions (l, d, and w). *Bondur and Sharkov* [1982] fitted a gamma distribution to their results for the areas of dynamic and static foams, but *Bortkovskii* [1987] encountered problems in fitting a gamma distribution to his data. Many more data points would be necessary to smooth the PDFs of the bubble cloud characteristics and establish functional formulations of their distributions.

[68] *Reul and Chapron* [2003] determined a distribution of foam thickness by relating a time-dependent model of foam layer thickness associated with an individual breaking wave (their equation 5) to wind-dependent whitecap fraction. Though the model is developed for surface foam layers (and

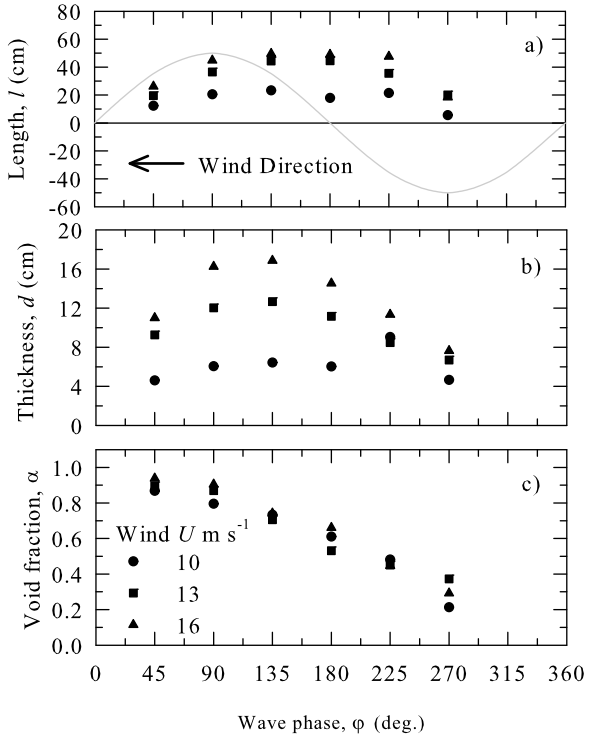

Figure 12. Bubble cloud characteristics relative to the wave phase φ at different wind speeds (10, 13, and 16 m s^{-1}, 10 realizations), side view: (a) bubble cloud length l, (b) bubble cloud thickness d, and (c) bubble cloud void fraction α. The gray line in Figure 12a is the profile of a regular sinusoidal wave.

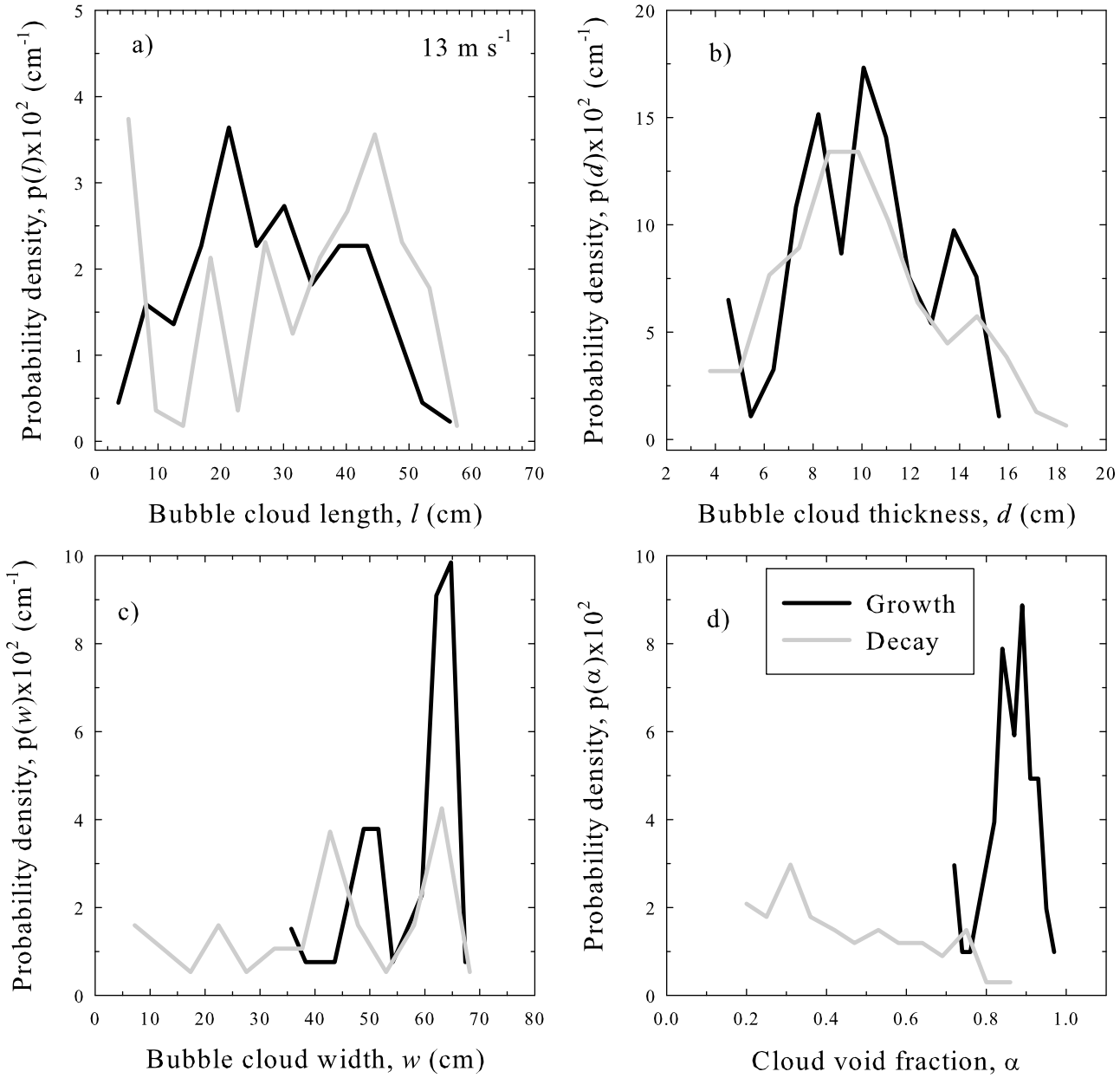

Figure 13. Probability density functions (PDFs) of bubble cloud characteristics at wind speed of 13 m s^{-1} in stages of growth (black lines) and decay (gray lines): (a) PDF for cloud length l (cm), (b) PDF for cloud thickness d (cm), (c) PDF for cloud width w (cm), and (d) PDF for cloud void fraction α.

not bubble clouds), its predictions are consistent with the most probable bubble cloud thickness measured in our experiments (Figure 13b). Specifically, they predict a foam layer thinner than 5 cm for breaking waves with $L < 1$ m. For the same L, we measure bubble cloud thickness no more than 20 cm.

5.6. Wind Speed Dependence of the Bubble Cloud Characteristics

[69] The effect of wind speed variations on the non-dimensional cloud thickness d/H_s and void fraction α are shown in Figure 15. Data are shown with mean values (averaged over growth or decay stages) and 95% confidence intervals. Non-dimensional cloud length and cloud width l/L and w/L have similar wind speed dependences (but are not shown for brevity). For the growth stage, the ratio d/H_s increases with the wind speed in a manner similar to that found by *Thorpe* [1982] (see section 5.4). For the decay stage, the trend is non-monotonic as d/H_s increases with U up to 12 m s^{-1} and decreases for higher wind speeds.

[70] Data for the cloud dimensions and their dependence on the wind speed are fitted with a power law in the form of $y \sim U^b$ where y represents l/L, d/H_s, w/L or α. The correlation coefficient for d/H_s in the growth stage is $r = 0.88$ (Figure 15a). Exponent b varies from 0.46 to 0.77 during the growth stage depending on the cloud characteristics (l/L, d/H_s, or w/L). The power law relationship is reported here because it is widely used to parameterize bubble size

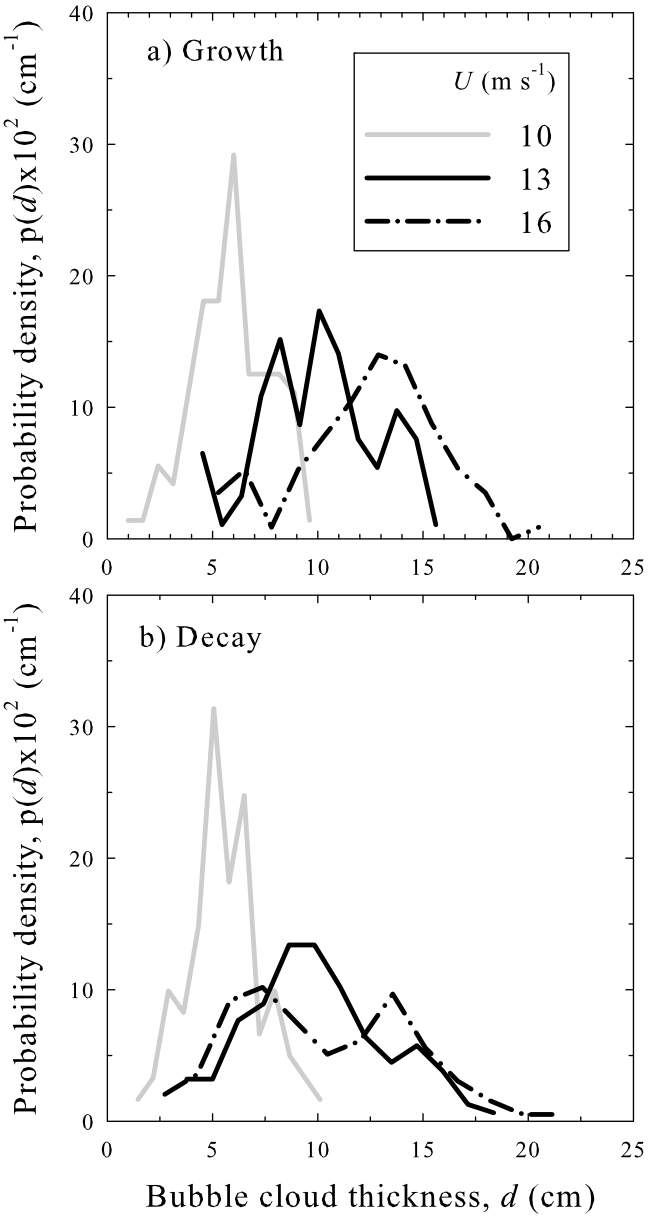

Figure 14. Probability density functions (PDFs) of bubble cloud thickness d at different wind speeds (10, 13, and 16 m s^{-1}) in stages of (a) growth and (b) decay.

distributions [e.g., *Leifer et al.*, 2006] and wind dependence of whitecap fraction [*Anguelova and Webster*, 2006, Table 1]. Note, however, that values of d/H_s level off for higher wind speeds. (The leveling off is even stronger for the dimensional data d.) We note that data are better parameterized by a logarithmic law in the form $y \sim \ln U$. The dependency of the void fraction on wind speed is weak (Figure 15b). The exponents b of the power law relationships for the growth and decay stages are 0.1 and 0.26, respectively, with correlation coefficients about 0.7.

6. Discussion

[71] Here we discuss the results presented in section 5 to gain further insights into bubble cloud dynamics and the applicability of the results to open ocean conditions.

6.1. Overlapping of Bubble Clouds

[72] For lower wind speeds (10–12 m s^{-1}), a bubble cloud completely dissipates before the next wave produces a new bubble cloud. At higher winds, degassing of the cloud leaves plumes with a residual void fraction of about 20%; these plumes continue to decay for more than one wave period. These are overlapped by new clouds formed by the next breaking wave. The decaying plumes are exposed to the influence of the next breaking wave and so experience stronger dynamic changes. Examination of Figure 10 shows that there is a large backward horizontal velocity V_x of the bubble cloud around 0.55 s (Figure 10a), against the wind speed direction. Such rapid backward movement of the bubble cloud in the wave trough (Figure 10c) is unexpected. However, it occurs repeatedly. For example, large backward motions occur for a different realization at 13 m s^{-1} (black symbols in Figure 16a); the realization shown in Figure 10a is repeated here for comparison (gray symbols). It also appears for a wind speed of 16 m s^{-1} (Figure 16b). An

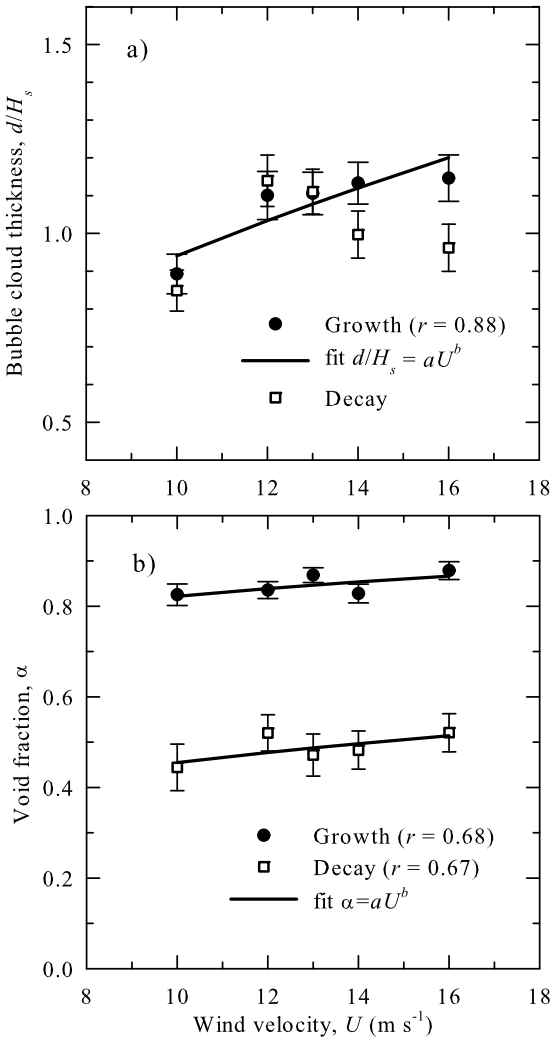

Figure 15. Wind dependence of the bubble cloud characteristics in growth (solid circles) and decay (open squares) stages: (a) cloud thickness scaled with significant wave height d/H_s and (b) cloud void fraction. The solid lines are a power law fit to the experimental points.

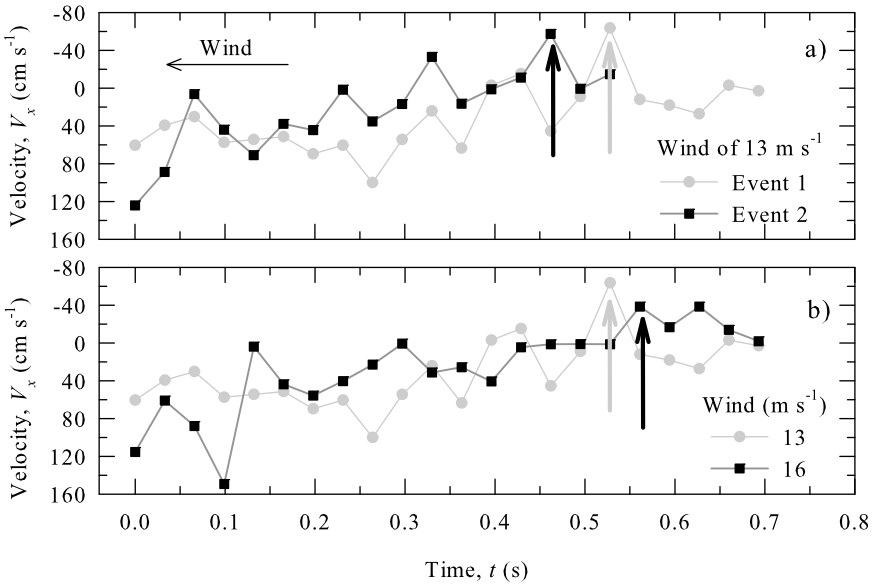

Figure 16. As Figure 10a for another bubble cloud realization (a) at 13 m s^{-1} and (b) at wind speed of 16 m s^{-1}. The data from Figure 10a are replotted in gray for comparison.

explanation of this observation is the strong "pull" of these decaying bubble plumes into the new incoming wave just before the breaking. The implication is that for higher wind speeds there is an interaction between the old or decaying and the new freshly generated bubble clouds.

6.2. Bubble Cloud Dynamics

[73] Wave breaking with air entrainment is one of the main mechanisms for dissipating the energy of wind-generated water waves [*Phillips*, 1985]. *Lamarre and Melville* [1991] report that up to 40% of the total wave energy is lost during the breaking event and that at least 30–50% of this dissipated energy is used to entrain air against buoyancy. Our results of the bubble cloud kinematics (section 5.3) suggest a complex interplay between the wave and buoyancy forcings. Estimates of the kinetic energy E_{kc} and the buoyancy E_b of the bubble cloud help us to understand how this interplay changes the relative contributions of the two forcings to the system dynamics at different lifetime stages of the bubble clouds.

[74] Wave forcing supplies the energy for creating the bubble cloud. One can use the wave height H to estimate the total wave energy density per unit area as $E = E_p + E_k = 2E_k \equiv 2E_p = (1/16)\rho g H^2$ [*Holthuijsen*, 2007], where E_k and E_p is the kinetic and potential energy, respectively. Employing our measured significant wave height H_s for H, we find $E_k = 2.8$ J m^{-2} at the wind speed of 13 m s^{-1} (Table 1). For the bubble cloud, the kinetic energy is $E_{kc} = (1/2)\rho_c V_c' . V^2$ and the buoyancy is $E_b = (\rho_c - \rho)V_c' g\Delta z = \Delta\rho_c V_c' g\Delta z$. Here ρ_c is the density of the air-water mixture; $V'_c = bld$ is the cloud volume (see section 4.2); V is the cloud velocity and Δz is vertical displacement. The motion of the cloud caused by E_b changes its kinetic energy, and thus at any moment E_{kc} comprises contributions from both the wave forcing and the cloud buoyancy.

[75] We calculate E_{kc} using $V^2 = V_x^2 + V_z^2$ in Figure 10, and E_b with Δz as the displacements between consecutive data points of the vertical trajectory of the bubble cloud (Figure 9b). We evaluate ρ_c as a linear combination of water and air densities using $\rho = 998.2$ kg m^{-3} and $\rho_a = 1.2$ kg m^{-3} (section 2.2) and void fraction representing the cloud density at $t = 0.3$ s, the moment separating the growth and decay stages (Figure 3). For a comparison to the wave energy density E, we use the cloud volume per unit area as $V_c'/(bl) = d$. We use $d/2$ in order to represent the thickness of one plume with local scales V and Δz (see section 4.2).

[76] Figure 17 shows the evolutions of E_{kc} and E_b during cloud growth and decay. The bubble cloud is entrained or pushed deep into the water by the breaking wave (Figure 9b) and possesses large horizontal velocity (Figure 10a) at small times $t_0 \sim 0$, thus the cloud energy is split between kinetic energy and buoyancy. Subsequently during the growth stage ($t \leq 0.45T$), E_b increases and the cloud moves upward toward the surface (Figure 9b). The buoyancy forcing is greater than E_{kc} for times up to about $0.4T$. The vertical motion of the cloud increases its kinetic energy, and E_{kc} becomes larger than E_b by the end of the growth stage at $t \approx 0.45T$.

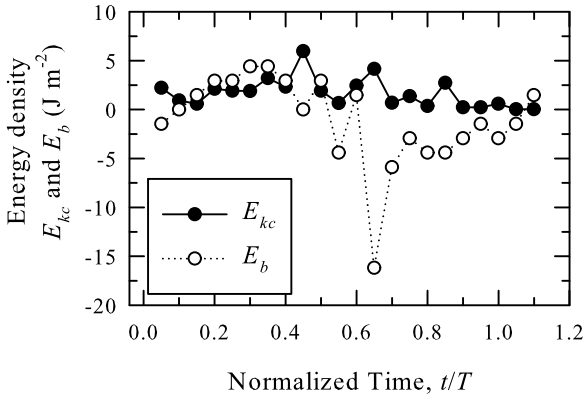

Figure 17. Estimates of the kinetic energy E_{kc} and the buoyancy E_b of the bubble cloud at 13 m s^{-1} shown in Figures 10–12 as a function of normalized time t/T.

[77] A noteworthy feature in the evolution of the cloud energy in the decaying stage ($t > 0.45T$) is the large negative buoyancy at $0.65T$ (Figure 17). At this moment, we observe fast downward displacement at wave phase of 150° ($\sim 0.65T$, Figure 9b). The cloud is still lighter than water despite its continuous degassing up to this moment, and there is no obvious reason for the downward movement. This suggests energy input from the wave. The magnitude of E_b steadily decreases toward the end of the decay stage. This yields small vertical velocities (Figure 10b) and slower downward motion (Figure 9b). The bubble cloud becomes nearly neutrally buoyant ($E_b \approx 0$) at the end of its lifetime. A perturbation in this quiescent stage is the effect of the next wave at $0.85T$ (section 6.1) seen in Figure 17 as a peak in the kinetic energy.

[78] On average (over the cloud lifetime), the energy needed to entrain air against the buoyancy is about E_b/E = 19%. This value is in the middle of the range of values previously reported—30–50% by *Lamarre and Melville* [1991] and up to 9% by *Blenkinsopp and Chaplin* [2007, Figure 11]. The evolution in Figure 17 is typical, and occurs at other wind speeds (section 5.3).

6.3. Turbulence due to Bubble Cloud

[79] *Thorpe* [1992] suggested that the bubbles can be used as tracers for the turbulence in the ocean. It would be informative to examine order of magnitude estimates of variables such as the vertical eddy diffusivity k_v and kinetic energy dissipation rate ε associated with turbulence generated by breaking waves.

[80] An estimate of eddy diffusivity is given by $k_v \propto L_s^2/\Delta T$, where L_s is the integral length scale characterizing the turbulence evolving over a time interval ΔT [*Tennekes and Lumley*, 1992]. The thickness of the bubble clouds d for the growth stage is a natural surrogate for L_s. The examination of the bubble cloud energy (section 6.2) showed that the buoyancy forcing dominates in the first third of the wave period. This results in energetic interaction between the wave and bubble cloud. A consequence is large rates of energy dissipation. To evaluate eddy diffusivity, we take $\Delta T = T/3 \sim 0.3$ s and d values for 10, 13, and 16 m s^{-1} wind speeds averaged for phase groups of 45° and 90° (Figure 12b), and obtain $k_v \cong 0.9 \times 10^{-2}$, 3.8×10^{-2}, and 6.2×10^{-2} m^2 s^{-1}, respectively.

[81] The magnitude of the dissipation rate can be estimated as $\varepsilon \propto u_s^3/L_s$, where $u_s \propto L_s/\Delta T$ is the effective turbulent velocity [*Tennekes and Lumley*, 1992]. Using again d values for the turbulent length scale and ΔT = 0.3 s, the estimates of the dissipation rate are $\varepsilon \cong 11 \times 10^{-2}$, 42×10^{-2}, 69×10^{-2} m^2 s^{-3} for wind speeds of 10, 13, and 16 m s^{-1}, respectively. These high ε estimates from our laboratory measurements are in good agreement with ε values obtained from lake data [*Gemmrich*, 2010, Figures 5 and 8]. Gemmrich's results not only confirmed the turbulence enhancement due to breaking waves [*Agrawal et al.*, 1992; *Terray et al.*, 1996], but were also the first demonstration with direct field observations that this enhancement is strongest in the region of the wave crest. Estimating ε using d values in the trough (Figure 12b) and the same interval of 0.3 s, we obtain dissipation rates ε lower than those in the crest by up to a factor of 3. Therefore, with our bubble cloud data and ε estimates, we provide laboratory confirmation that enhanced turbulence under breaking waves is predominantly localized in the wave crests.

6.4. Open Ocean Applicability

[82] Extrapolation of laboratory results to open ocean conditions is not straightforward because of the limited range of wind-forcing and incomplete simulation of the wavefield in laboratory wind-wave tanks. For example, the behavior of the wave spectrum as the wind increased in the tank was similar to that observed in other experiments (section 5.1). However, the magnitude of change was relatively small with peak frequency differing by only 20% (from 1.67 Hz to 1.34 Hz) as the wind speed varied from 9 m s^{-1} to 16 m s^{-1}. The wavelength of the dominant wave ranged from 0.56 m to 0.87 m in our experiment (Table 1). The dominant wave in the ocean is much longer and higher (by one or two orders of magnitude) than in the tank at 16 m s^{-1} or any other of the studied wind speeds [e.g., *Lamarre and Melville*, 1992, Table 1; *Taylor and Yelland*, 2001]. In addition, the reported bubble cloud characteristics are for a fixed fetch of 26 m. A strong fetch dependence for bubble plume formation was observed by *Leifer et al.* [2006] in the laboratory, and reported for whitecaps in the field [*Xu et al.*, 2000; *Zhao and Toba*, 2001; *Piazzola et al.*, 2002; *Lafon et al.*, 2004]. This points to fetch as a key variable that influences the wavefield.

[83] Laboratory data are often scaled in order to either extrapolate them to open ocean conditions or to compare them to other published results. Two scaling approaches have been used to extend laboratory data D_{lab} to the ocean (i.e., D_{open}). One scaling approach is to multiply D_{lab} with a parameter formulated on physical grounds P_{phys} and involving some forcing variables, e.g., $D_{\text{open}} = P_{\text{phys}}(U_{10}) \times D_{\text{lab}}$, where U_{10} is the wind speed at a 10-m reference height [e.g., *Anguelova et al.*, 1999; *Fairall et al.*, 2009, section 3]. Another scaling approach is to normalize one variable D_{lab} of a complex system (e.g., bubble cloud in wavefield) with a relevant, reference variable D_{lab0} to obtain a scaling ratio $D_{\text{lab}}/D_{\text{lab0}}$ [e.g., *Bonmarin*, 1989; *Lamarre and Melville*, 1994]. Assuming similarity between the simulated and oceanic versions of this complex system, one expects equality between their scaling ratios (scale invariance), i.e., $D_{\text{lab}}/D_{\text{lab0}} = D_{\text{open}}/D_{\text{open0}}$. *Fairall et al.* [2009] review various scaling arguments and note that each approach has caveats.

[84] Our results illustrate both the limitation and usefulness of the normalization approach for extrapolation. The lack of strict scale invariance between the laboratory and field can be explained by the inability of laboratory wind-wave tanks to simulate the multiple and larger scales of the wavefield in the open ocean. It is likely that the much longer breaking waves occurring in the open ocean at the studied wind speed values will modify the statistical distribution of bubble clouds (section 5.5) and their wind speed dependence (section 5.6). Furthermore, the fetch effect on the wavefield in the open ocean will complicate the analysis of bubble cloud characteristics.

[85] The cloud thicknesses observed in the laboratory, from $0.7H_s$ to $1.5H_s$ (section 5.4), compare favorably with *Thorpe*'s [1992] field observations of cloud entrainment (section 2.2). Our result for $l/L < 1$ also conforms to field observations [*Bortkovskii*, 1987] (section 5.4). The bubble cloud velocity (section 5.3) is comparable to that measured by *Bezzabotnov et al.* [1986] (section 2.2). Void fractions observed in the laboratory are comparable to those observed by *Deane* [1997] in the surf zone (section 2.2). Such agreement between the

laboratory and field data suggests that at least to some extent the characteristics of the bubble clouds and the wavefield created in the laboratory reflect those of bubble clouds and wavefield in the open ocean.

[86] Our results are for water temperature of 20°C and fresh water. Thus, bubble cloud characteristics observed in our laboratory study may differ from those in the open ocean because of environmental factors such as water temperature, salinity, and surfactants [*Monahan and O'Muircheartaigh*, 1986; *de Leeuw et al.*, 2011]. For example, temperature and salinity variations affect the bubble size distribution and may alter the wind dependence of whitecap fraction [*Bortkovskii*, 1987; *Stramska and Petelski*, 2003; *Monahan and Zietlow*, 1969; *Cartmill and Su*, 1993]. In this context, extrapolation of our result concerning the persistence of residual void fraction for $O(100)$ wave periods (section 5.2) to the open ocean should be viewed with caution for two reasons, the use of fresh water, and the limited water depth and width of the laboratory tank. This, coupled with the patchy pattern of wave breaking in the ocean, may lead to less clustering of bubbles in one location from multiple breaking waves and attenuated persistence of the residual void fraction. We are investigating the effects of the water temperature and salinity on bubble cloud characteristics with additional laboratory experiments; the results will be reported in forthcoming papers.

7. Conclusions

[87] The results of a laboratory study on bubble cloud characteristics under wind speeds of 9–16 m s^{-1} are reported. A photographic technique was employed to record bubble cloud events in side and top views. Careful illumination and image processing allows measurement of bubble cloud characteristics from images where the bubbles are represented by bright pixels. Time series for bubble cloud dimensions (length l, thickness d, width w) and void fraction α were successfully extracted from the images. Complementary measurements of water surface elevation were made for scaling of the bubble cloud characteristics with the dominant wave parameters (frequency f, period T, wavelength L, and phase speed c, and significant wave height H_s). Conclusions of the study are as follows:

[88] 1. The bubble clouds form, grow and decay over approximately a wave period; the temporal variations of all bubble cloud dimensions (length, thickness, and width) reflect this evolution.

[89] 2. The bubble cloud lifetime—comprising formation, growth, and decay—is of the order of the wave period, but shows considerable variability. For example, at lowest (10 m s^{-1}) and highest (16 m s^{-1}) winds both short $O(0.6T)$ and long $O(1T)$ cloud lifetimes are possible.

[90] 3. The bubble cloud moves forward horizontally with the wave for the initial 1/3 of the wave period at approximately half the wave phase speed ($0.5c$). The wave forcing decreases in the wave trough when the horizontal velocity of the bubble cloud diminishes to almost zero, and the dominant motion is vertical with an average speed about half that of rising bubbles.

[91] 4. Estimation of the void fraction of bubble clouds from images representing the bubbles as bright pixels is feasible. Future work should consider rigorous calibration of the number of bright pixels and the void fraction.

[92] 5. The void fraction α changes significantly during the lifetime of the bubble cloud. It could be as high as 80–99% in the first quarter ($0.25T$) of the bubble cloud lifetime (wave phase φ up to 90°). The void fraction decreases steadily to about 20–30% at $0.7T$ ($\varphi \sim 270°$). Residual void fractions can persist for long times $O(100T)$.

[93] 6. Probability density functions (PDFs) of the bubble cloud characteristics show that the bubble cloud length varies from $0.1L$ to $0.7L$. The bubble cloud thickness assumes values from $0.5H_s$ to $2H_s$. The bubble cloud characteristics have different ranges of values for the growth and decay stages of the bubble cloud evolution.

[94] 7. Bubble cloud dimensions scaled with the wave parameters and also the cloud void fraction shows a weak dependence on wind speed for the growth stage. Power or logarithmic laws can be used to parameterize the wind dependence in the growth stage. For the decay stage, the scaled bubble cloud dimensions vary non-monotonically with increasing wind speed.

[95] **Acknowledgments.** The authors acknowledge the help of colleagues at the Air-Sea Interaction Laboratory, University of Delaware, at the time of collection of the data reported here. We also thank Andrey Savtchenko and two anonymous reviewers for helpful comments. Part of this work is sponsored by the Office of Naval Research (NRL program element 61153N) and the National Science Foundation.

References

Agrawal, Y. C., E. A. Terray, M. A. Donelan, P. A. Hwang, A. J. Williams III, W. M. Drennan, K. K. Kahma, and S. A. Krtaigorodskii (1992), Enhanced dissipation of kinetic energy beneath surface waves, *Nature*, *359*, 219–220, doi:10.1038/359219a0.

Andreas, E. L., P. P. G. Persson, and J. E. Hare (2008), A bulk turbulent air-sea flux algorithm for high-wind, spray conditions, *J. Phys. Oceanogr.*, *38*, 1581–1596, doi:10.1175/2007JPO3813.1.

Anguelova, M. D., and F. Webster (2006), Whitecap coverage from satellite measurements: A first step toward modeling the variability of oceanic whitecaps, *J. Geophys. Res.*, *111*, C03017, doi:10.1029/2005JC003158.

Anguelova, M. D., R. P. Barber, and J. Wu (1999), Spume drops produced by the wind tearing of wave crests, *J. Phys. Oceanogr.*, *29*, 1156–1165, doi:10.1175/1520-0485(1999)029<1156:SDPBTW>2.0.CO;2.

Asher, W., and R. Wanninkhof (1998), The effects of bubble-mediated gas transfer on purposeful dual-gaseous tracer experiment, *J. Geophys. Res.*, *103*, 10,555–10,560, doi:10.1029/98JC00245.

Babanin, A. V. (2009), Breaking of ocean surface waves, *Acta Phys. Slovaca*, *59*(4), 305–535.

Babanin, A., D. Chalikov, I. Young, and I. Savelyev (2007), Predicting the breaking onset of surface water waves, *Geophys. Res. Lett.*, *34*, L07605, doi:10.1029/2006GL029135.

Banner, M. L., I. S. F. Jones, and J. C. Trinder (1989), Wavenumber spectra of short gravity waves, *J. Fluid Mech.*, *198*, 321–344, doi:10.1017/S0022112089000157.

Bezzabotnov, V. S. (1985), Certain results of field measurements of the structure of sea-foam formation, *Izv. Acad. Sci. USSR Atmos. Oceanic Phys.*, *21*(1), 77–79.

Bezzabotnov, V. S., R. S. Bortkovskii, and D. F. Timanovskiy (1986), On the structure of the two-phase medium formed when wind waves break (1985), *Izv. Acad. Sci. USSR Atmos. Oceanic Phys.*, *22*(11), 922–928.

Blanchard, D. C. (1963), The electrification of the atmosphere by particles from bubbles in the sea, *Prog. Oceanogr.*, *1*, 71–202, doi:10.1016/0079-6611(63)90004-1.

Blenkinsopp, C. E., and J. R. Chaplin (2007), Void fraction measurements in breaking waves, *Proc. R. Soc. A*, *463*, 3151–3170, doi:10.1098/rspa.2007.1901.

Bondur, V. G., and E. A. Sharkov (1982), Statistical properties of whitecaps on a rough sea, *Oceanology*, *22*, 274–279.

Bonmarin, P. (1989), Geometric properties of deep-water breaking waves, *J. Fluid Mech.*, *209*, 405–433, doi:10.1017/S0022112089003162.

Bortkovskii, R. S. (1987), *Air-Sea Exchange of Heat and Moisture During Storms*, Reidel, Dordrecht, Netherlands.

Camps, A., et al. (2005), The emissivity of foam-covered water surface at L-band: Theoretical modeling and experimental results from the FROG 2003 field experiment, *IEEE Trans. Geosci. Remote Sens.*, *43*, 925–937, doi:10.1109/TGRS.2004.839651.

Carey, W. M., J. W. Fitzgerald, E. C. Monahan, and Q. Wang (1993), Measurement of the sound produced by a tipping trough with fresh and salt water, *J. Acoust. Soc. Am.*, *93*(6), 3178–3192, doi:10.1121/1.405702.

Cartellier, A. (1990), Optical probes for local void fraction measurements: Characterization of performance, *Rev. Sci. Instrum.*, *61*(2), 874–886, doi:10.1063/1.1141457.

Cartmill, J., and M. Su (1993), Bubble size distribution under saltwater and freshwater breaking waves, *Dyn. Atmos. Oceans*, *20*, 25–31, doi:10.1016/0377-0265(93)90046-A.

Clift, R., J. R. Grace, and M. E. Weber (1978), *Bubbles, Drops, and Particles*, Academic, San Diego, Calif.

Dahl, P. H., and A. T. Jessup (1995), On bubble clouds produced by breaking waves: An event analysis of ocean acoustic measurements, *J. Geophys. Res.*, *100*(C3), 5007–5020, doi:10.1029/94JC03019.

Deane, G. B. (1997), Sound generation and air entrainment by breaking waves in the surf zone, *J. Acoust. Soc. Am.*, *102*(5), 2671–2689, doi:10.1121/1.420321.

Deane, G. B., and M. D. Stokes (1999), Air entrainment processes and bubble size distributions in the surf zone, *J. Phys. Oceanogr.*, *29*(7), 1393–1403, doi:10.1175/1520-0485(1999)029<1393:AEPABS>2.0.CO;2.

de Leeuw, G., E. Andreas, M. D. Anguelova, C. Fairall, E. Lewis, C. O'Dowd, M. Schulz, and S. Schwartz (2011), Production flux of sea spray aerosol, *Rev. Geophys.*, *49*, RG2001, doi:10.1029/2010RG000349.

Fairall, C., J. Keppert, and G. Holland (1994), The effect of sea spray on surface energy transport over the ocean, *Global Atmos. Ocean Syst.*, *2*, 121–142.

Fairall, C. W., M. L. Banner, W. L. Peirson, W. Asher, and R. P. Morison (2009), Investigation of the physical scaling of sea spray spume droplet production, *J. Geophys. Res.*, *114*, C10001, doi:10.1029/2008JC004918.

Forristall, G. Z. (1981), Measurements of a saturated range in ocean wave spectra, *J. Geophys. Res.*, *86*, 8075–8084, doi:10.1029/JC086iC09p08075.

Frouin, R., M. Schwindling, and P.-Y. Deschamps (1996), Spectral reflectance of sea foam in the visible and near-infrared: In situ measurements and remote sensing implications, *J. Geophys. Res.*, *101*, 14,361–14,371, doi:10.1029/96JC00629.

Gemmrich, J. (2010), Strong turbulence in the wave crest region, *J. Phys. Oceanogr.*, *40*, 583–595, doi:10.1175/2009JPO4179.1.

Gemmrich, J. R., M. L. Banner, and C. Garrett (2008), Spectrally resolved energy dissipation rate and momentum flux of breaking waves, *J. Phys. Oceanogr.*, *38*, 1296–1312, doi:10.1175/2007JPO3762.1.

Gordon, H. R., and M. Wang (1994), Influence of oceanic whitecaps on atmospheric correction of ocean-color sensors, *Appl. Opt.*, *33*(33), 7754–7763, doi:10.1364/AO.33.007754.

Griffin, O. M., R. D. Peltzer, H. T. Wang, and W. W. Schultz (1996), Kinematic and dynamic evolution of deep water breaking waves, *J. Geophys. Res.*, *101*(C7), 16,515–16,531, doi:10.1029/96JC00281.

Holthuijsen, L. H. (2007), *Waves in Oceanic and Coastal Waters*, Cambridge Univ. Press, Cambridge, U. K., doi:10.1017/CBO9780511618536.

Kalvoda, P. M., L. Xu, and J. Wu (2003), Macrobubble clouds produced by breaking wind waves: A laboratory study, *J. Geophys. Res.*, *108*(C6), 3207, doi:10.1029/1999JC000265.

Kennedy, R. M., and R. L. Snyder (1983), On the formation of whitecaps by a threshold mechanism. Part II: Monte Carlo experiments, *J. Phys. Oceanogr.*, *13*, 1493–1504, doi:10.1175/1520-0485(1983)013<1493:OTFOWB>2.0.CO;2.

Koepke, P. (1986), Remote sensing signatures of whitecaps, in *Oceanic Whitecaps*, edited by E. C. Monahan and G. M. Niocaill, pp. 251–260, Reidel, Dordrecht, Netherlands, doi:10.1007/978-94-009-4668-2_23.

Koga, M. (1982), Bubble entrainment in breaking wind waves, *Tellus A*, *34*, 481–489, doi:10.1111/j.2153-3490.1982.tb01836.x.

Kraan, C., W. Oost, and P. Janssen (1996), Wave energy dissipation by whitecaps, *J. Atmos. Oceanic Technol.*, *13*, 262–267, doi:10.1175/1520-0426(1996)013<0262:WEDBW>2.0.CO;2.

Lafon, C., J. Piazzola, P. Forget, O. le Calve, and S. Despiau (2004), Analysis of the variations of the whitecap fraction as measured in a coastal zone, *Boundary Layer Meteorol.*, *111*, 339–360, doi:10.1023/B:BOUN.0000016490.83880.63.

Lamarre, E., and W. K. Melville (1991), Air entrainment and dissipation in breaking waves, *Nature*, *351*, 469–472, doi:10.1038/351469a0.

Lamarre, E., and W. K. Melville (1992), Instrumentation for the measurement of void-fraction in breaking waves: Laboratory and field results, *IEEE J. Oceanic Eng.*, *17*(2), 204–215, doi:10.1109/48.126977.

Lamarre, E., and W. K. Melville (1994), Void-fraction measurements and sound-speed fields in bubble plumes generated by breaking waves, *J. Acoust. Soc. Am.*, *95*(3), 1317–1328, doi:10.1121/1.408572.

Leifer, I., and G. de Leeuw (2006), Bubbles generated from wind-steepened breaking waves: 1. Bubble plume bubbles, *J. Geophys. Res.*, *111*, C06020, doi:10.1029/2004JC002673.

Leifer, I., G. de Leeuw, and L. H. Cohen (2003a), Optical measurement of bubbles: System design and application, *J. Atmos. Oceanic Technol.*, *20*(9), 1317–1332, doi:10.1175/1520-0426(2003)020<1317:OMOBSD>2.0.CO;2.

Leifer, I., G. de Leeuw, G. Kunz, and L. H. Cohen (2003b), Calibrating optical bubble size by the displaced-mass method, *Chem. Eng. Sci.*, *58*, 5211–5216, doi:10.1016/j.ces.2003.08.016.

Leifer, I., G. Caulliez, and G. de Leeuw (2006), Bubbles generated from wind-steepened breaking waves: 2. Bubble plumes, bubbles, and wave characteristics, *J. Geophys. Res.*, *111*, C06021, doi:10.1029/2004JC002676.

Lewis, E. R., and S. E. Schwartz (Eds.) (2004), *Sea Salt Aerosol Production: Mechanisms Methods Measurements and Models—A Critical Review*, *Geophys. Monogr. Ser.*, vol. 152, 413 pp., AGU, Washington, D. C., doi:10.1029/GM152.

Loewen, M. R., M. A. O'Dor, and M. G. Skafel (1996), Bubbles entrained by mechanically generated breaking waves, *J. Geophys. Res.*, *101*(C9), 20,759–20,769, doi:10.1029/96JC01919.

Longuet-Higgins, M. S. (1990), An effect of sidewalls on waves in a wind wave channel, *J. Geophys. Res.*, *95*, 1765, doi:10.1029/JC095iC02p01765.

Longuet-Higgins, M. S., and J. S. Turner (1974), An 'entraining plume' model of a spilling breaker, *J. Fluid Mech.*, *63*(1), 1–20, doi:10.1017/S002211207400098X.

Massel, S. R. (2007), *Ocean Waves Breaking and Marine Aerosol Fluxes*, Springer, New York.

Medwin, H., and N. D. Breitz (1989), Ambient and transient bubble spectral densities in quiescent seas and under spilling breakers, *J. Geophys. Res.*, *94*, 12,751–12,759, doi:10.1029/JC094iC09p12751.

Melville, W. K. (1983), Wave modulation and breakdown, *J. Fluid Mech.*, *128*, 489–506, doi:10.1017/S0022112083000579.

Melville, W. K. (1994), Energy dissipation by breaking waves, *J. Phys. Oceanogr.*, *24*, 2041–2049, doi:10.1175/1520-0485(1994)024<2041:EDBBW>2.0.CO;2.

Melville, W. K. (1996), The role of surface-wave breaking in air-sea interaction, *Annu. Rev. Fluid Mech.*, *28*, 279–321, doi:10.1146/annurev.fl.28.010196.001431.

Melville, W. K., E. Terrill, and L. Ding (1995), Field measurements of air entrainment by breaking waves, in *Air-Water Gas Transfer*, edited by B. Jähne and E. C. Monahan, pp. 285–295, AEON, Hanau, Germany.

Mitsuyasu, H. (1977), Measurements of the high-frequency spectrum of ocean surface waves, *J. Phys. Oceanogr.*, *7*, 882–891, doi:10.1175/1520-0485(1977)007<0882:MOTHFS>2.0.CO;2.

Mitsuyasu, H., and T. Honda (1974), The high frequency spectrum of wind-generated waves, *J. Oceanogr.*, *30*, 185–198.

Monahan, E. (1993), Occurrence and evolution of acoustically relevant subsurface bubble plumes and their associated, remotely monitorable, surface whitecaps, in *Natural Physical Sources of Underwater Sound*, edited by B. Kerman, pp. 503–517, Kluwer, Dordrecht, Netherlands, doi:10.1007/978-94-011-1626-8_37.

Monahan, E. C., and M. Lu (1990), Acoustically relevant bubble assemblages and their dependence on meteorological parameters, *IEEE J. Oceanic Eng.*, *15*, 340–349, doi:10.1109/48.103530.

Monahan, E. C., and I. G. O'Muircheartaigh (1986), Whitecaps and the passive remote-sensing of the ocean surface, *Int. J. Remote Sens.*, *7*(5), 627–642, doi:10.1080/01431168608954716.

Monahan, E., and C. Zietlow (1969), Laboratory comparisons of fresh-water and salt-water whitecaps, *J. Geophys. Res.*, *74*, 6961–6966, doi:10.1029/JC074i028p06961.

Monahan, E. C., K. L. Davidson, and D. E. Spiel (1982), Whitecap aerosol productivity deduced from simulation tank measurements, *J. Geophys. Res.*, *87*(C11), 8898–8904, doi:10.1029/JC087iC11p08898.

Monahan, E. C., Q. Wang, X. Wang, and M. B. Wilson (1994), Air entrainment by breaking waves: A laboratory assessment, in *Aeration Technology*, edited by R. E. A. Arndt and A. Prosperetti, pp. 21–26, Am. Soc. of Mech. Eng., New York.

Nordberg, W., J. Conaway, D. Ross, and T. Wilheit (1971), Measurements of microwave emission from a foam-covered, wind-driven sea, *J. Atmos. Sci.*, *28*, 429–435, doi:10.1175/1520-0469(1971)028<0429:MOMEFA>2.0.CO;2.

Ochi, M. K., and C.-H. Tsai (1983), Prediction of occurrence of breaking waves in deep water, *J. Phys. Oceanogr.*, *13*, 2008–2019, doi:10.1175/1520-0485(1983)013<2008:POOOBW>2.0.CO;2.

Odelevskiy, V. I. (1951), Calculation of generalized conductance of heterogeneous systems. Part 1: Matrix two phase systems with nonelongated inclusions, *Zh. Tekh. Fiz.*, *21*, 667–685.

Phillips, O. (1985), Spectral and statistical properties of the equilibrium range in wind-generated gravity waves, *J. Fluid Mech.*, *156*, 505–531, doi:10.1017/S0022112085002221.

Piazzola, J., P. Forget, and S. Despiau (2002), A sea spray generation function for fetch-limited conditions, *Ann. Geophys.*, *20*, 121–131, doi:10.5194/angeo-20-121-2002.

Prosperetti, A. (1988), Bubble-related ambient noise in the ocean, *J. Acoust. Soc. Am.*, *84*, 1042–1054, doi:10.1121/1.396740.

Rapp, R. J., and W. K. Melville (1990), Laboratory measurements of deep-water breaking waves, *Philos. Trans. R. Soc. London, Ser. A*, *331*, 735–800, doi:10.1098/rsta.1990.0098.

Reul, N., and B. Chapron (2003), A model of sea-foam thickness distribution for passive microwave remote sensing applications, *J. Geophys. Res.*, *108*(C10), 3321, doi:10.1029/2003JC001887.

Rojas, G., and M. R. Loewen (2007), Fiber-optic probe measurements of void fraction and bubble size distributions beneath breaking waves, *Exp. Fluids*, *43*, 895–906, doi:10.1007/s00348-007-0356-5.

Rojas, G., and M. R. Loewen (2010), Void fraction measurements beneath plunging and spilling breaking waves, *J. Geophys. Res.*, *115*, C08001, doi:10.1029/2009JC005614.

Stansell, P., and C. MacFarlane (2002), Experimental investigation of wave breaking criteria based on wave phase speeds, *J. Phys. Oceanogr.*, *32*, 1269–1283, doi:10.1175/1520-0485(2002)032<1269:EIOWBC>2.0.CO;2.

Stokes, M. D., and G. B. Deane (1999), A new optical instrument for the study of bubbles at high void fractions within breaking waves, *IEEE J. Oceanic Eng.*, *24*(3), 300–311, doi:10.1109/48.775292.

Stramska, M., and T. Petelski (2003), Observations of oceanic whitecaps in the north polar waters of the Atlantic, *J. Geophys. Res.*, *108*(C3), 3086, doi:10.1029/2002JC001321.

Stramska, M., R. Marks, and E. C. Monahan (1990), Bubble-mediated aerosol production as a consequence of wave breaking in supersaturated (hyperoxic) seawater, *J. Geophys. Res.*, *95*(C10), 18,281–18,288, doi:10.1029/JC095iC10p18281.

Su, M. Y., D. Todoroff, and J. Cartmill (1994), Laboratory comparisons of acoustic and optical sensors for microbubble measurement, *J. Atmos. Oceanic Technol.*, *11*(1), 170–181, doi:10.1175/1520-0426(1994)011<0170:LCOAAO>2.0.CO;2.

Sugihara, Y., H. Tsumori, T. Ohga, H. Yoshioka, and S. Serizawa (2007), Variation of whitecap coverage with wave-field conditions, *J. Mar. Syst.*, *66*, 47–60, doi:10.1016/j.jmarsys.2006.01.014.

Swift, C. T. (1990), Passive microwave remote sensing of ocean surface wind speed, in *Surface Waves and Fluxes*, vol. II, edited by G. L. Geernaert and W. J. Plant, pp. 265–292, Kluwer Acad., Dordrecht, Netherlands.

Taylor, P. K., and M. J. Yelland (2001), The dependence of sea surface roughness on the height and steepness of the waves, *J. Phys. Oceanogr.*, *31*, 572–590, doi:10.1175/1520-0485(2001)031<0572:TDOSSR>2.0.CO;2.

Tennekes, H., and J. L. Lumley (1992), *A First Course in Turbulence*, MIT Press, Cambridge, Mass.

Terray, E. A., M. A. Donelan, Y. C. Agrawal, W. M. Drennan, K. K. Kahma, A. J. Williams, P. A. Hwang, and S. A. Kitaigorodskii (1996), Estimates of kinetic energy dissipation under breaking waves, *J. Phys. Oceanogr.*, *26*, 792–807, doi:10.1175/1520-0485(1996)026<0792:EOKEDU>2.0.CO;2.

Terrill, E., and W. K. Melville (1997), Sound-speed measurements in the surface-wave layer, *J. Acoust. Soc. Am.*, *102*(5), 2607–2625, doi:10.1121/1.420315.

Thorpe, S. A. (1982), On the clouds of bubbles formed by breaking wind-waves in deep water, and their role in air-sea gas transfer, *Philos. Trans. R. Soc. London, Ser. A*, *304*, 155–210, doi:10.1098/rsta.1982.0011.

Thorpe, S. A. (1992), Bubble clouds and the dynamics of the upper ocean, *Q. J. R. Meteorol. Soc.*, *118*, 1–22, doi:10.1002/qj.49711850302.

Toffoli, A., A. Babanin, M. Onorato, and T. Waseda (2010), Maximum steepness of oceanic waves: Field and laboratory experiments, *Geophys. Res. Lett.*, *37*, L05603, doi:10.1029/2009GL041771.

Vagle, S., and D. M. Farmer (1992), The measurement of bubble-size distributions by acoustical backscatter, *J. Atmos. Oceanic Technol.*, *9*(5), 630–644, doi:10.1175/1520-0426(1992)009<0630:TMOBSD>2.0.CO;2.

Vagle, S., and D. M. Farmer (1998), A comparison of four methods for bubble size and void fraction measurements, *IEEE J. Oceanic Eng.*, *23*(3), 211–222, doi:10.1109/48.701193.

Walsh, A. L., and P. J. Mulhearn (1987), Photographic measurements of bubble populations from breaking wind-waves at sea, *J. Geophys. Res.*, *92*(C13), 14,553–14,565, doi:10.1029/JC092iC13p14553.

Wanninkhof, R., W. E. Asher, D. T. Ho, C. Sweeney, and W. R. McGillis (2009), Advances in quantifying air-sea gas exchange and environmental forcing, *Annu. Rev. Mar. Sci.*, *1*, 213–244, doi:10.1146/annurev.marine.010908.163742.

Woolf, D. K. (1993), Bubbles and the air-sea transfer velocity of gases, *Atmos. Ocean*, *31*, 517–540, doi:10.1080/07055900.1993.9649484.

Xu, D., P. A. Hwang, and J. Wu (1986), Breaking of wind-generated waves, *J. Phys. Oceanogr.*, *16*, 2172–2178, doi:10.1175/1520-0485(1986)016<2172:BOWGW>2.0.CO;2.

Xu, D., X. Liu, and D. Yu (2000), Probability of wave breaking and whitecap coverage in a fetch-limited sea, *J. Geophys. Res.*, *105*, 14,253–14,259, doi:10.1029/2000JC900040.

Zhao, D., and Y. Toba (2001), Dependence of whitecap coverage on wind and wind-wave properties, *J. Oceanogr.*, *57*, 603–616, doi:10.1023/A:1021215904955.

M. D. Anguelova, Remote Sensing Division, Naval Research Laboratory, Code 7223, 4555 Overlook Ave. SW, Washington, DC 20375-5320, USA. (maggie.anguelova@nrl.navy.mil)

P. Huq, College of Earth, Ocean, and Environment, University of Delaware, 205 Robinson Hall, Newark, DE 19716, USA.